breast cancer as the target disease for investigation of the MT1-MMP probe.

MATERIALS AND METHODS

Cell Lines and Animal Models Female C3H/He mice (5 weeks old), supplied by Japan SLC, Inc. (Hamamatsu, Japan), were housed under a 12 h light/12 h dark cycle and were given free access to a biotin-deficient diet and water. The animal experiments in this study were conducted in accordance with institutional guidelines and approved by the Kyoto University Animal Care Committee, Japan.

The mouse breast carcinoma FM3A cell line, supplied by Health Science Research Resources Bank (Osaka, Japan), was used for the preparation of tumor-bearing animal models. The cells were grown in Dulbecco's modified Eagle's medium (Nissui Pharmaceutical Co., Japan) containing 10% fetal bovine serum and were maintained in a humidified atmosphere of 5% CO_2 and 95% air at 37 °C with a 10.6 h doubling time.

FM3A cells were suspended in 0.01 M phosphate buffered saline (PBS) (pH 7.4) followed by subcutaneous inoculation into the right thigh of mice (5×10^6 cells/100 μl PBS/mouse). Individual tumor volumes (V) were estimated as $V=ab^2/2$, where a is the larger diameter and b is the smaller diameter.[15] Biodistribution studies were performed 7—8 d after implantation. The tumor volume was 155 ± 78 mm^3. The expression of MT1-MMP in FM3A cells and tumor tissues was confirmed by western blotting and immunohistochemistry.[8]

Synthesis of Biotinylated Anti-MT1-MMP mAb Anti-MT1-MMP mAb (113-5B7, Daiichi Fine Chemical Co., Japan), a purified mouse monoclonal IgG_3 to an oligopeptide, residues 319 to 333 of human MT1-MMP numbered from the signal peptide, was used for experiments after purification with a HiTrap rProtein A column (GE Healthcare, U.K.). Since the amino acid sequence of the MT1-MMP protein is highly conserved among species including mouse, rat, rabbit, and human,[16] this antibody can cross-react with mouse as well as human MT1-MMP.[17]

EZ-Link® sulfosuccinimidyl-6-(biotinamido) hexanoate (sulfo-NHS-LC-biotin) (Pierce, Inc., U.S.A.) (105 μl, 1.0 mg/ml in 0.1 M PBS (pH 7.4)) was added to a solution of anti-MT1-MMP mAb (2.4 ml, 1.0 mg/ml in 0.1 M PBS (pH 7.4)) in a molar ratio of 12 : 1. The mixture was gently stirred for 30 min at room temperature and then was purified with a diafiltration membrane (Amicon Ultra 4 (MWCO 30000), Millipore Co., U.S.A.). The mean substitution ratio for biotin molecules coupled to the antibody was determined by the EZ™ Biotin Quantitation Kit (Pierce, Inc.) using 4-hydroxyazobenzene-2′-carboxylic acid (HABA). The immunoreactivity of biotinylated anti-MT1-MMP mAb was measured using flow cytometry as previously described.[18] In brief, the antibody (50 μg/ml, 100 μl) (anti-MT1-MMP mAb, biotinylated anti-MT1-MMP mAb or negative control IgG_3 (sc-3880, Santa Cruz Biotechnology, Inc., U.S.A.) was added to mouse macrophage cells (RAW264.7, 2×10^6 cells) and was incubated for 30 min on ice, followed by incubation with FITC-Alexa-Fluor® 488 goat anti-mouse IgG antibody (A-11001, Molecular Probes, Inc., U.S.A.) (10 μg/ml, 100 μl) for 30 min on ice. The fluorescence level was measured using a flow cytometer (Becton Dickinson Inc., U.S.A.), and the data were analyzed using BD CellQuest Pro (BD Biosciences Inc., U.S.A.). An index of immunoreactivity for the anti-MT1-MMP mAb and biotinylated anti-MT1-MMP mAb was calculated by the following equation: median fluorescence intensity of anti-MT1-MMP mAb or biotinylated anti-MT1-MMP mAb divided by median fluorescence intensity of the negative control IgG.

Preparation and Purification of Anti-MT1-MMP mAb-SAv Conjugate A solution of biotinylated anti-MT1-MMP mAb (1.93 ml, 1 mg/ml in PBS) was added to a solution of streptavidin (SAv) (2.32 mg) (Pierce, Inc.) in a 1 : 3 molar ratio. The mixture was incubated for 1 h at 37 °C followed by purification twice by affinity chromatography using a HiTrap rProtein A column. The eluate containing anti-MT1-MMP mAb-SAv was concentrated with a diafiltration membrane (MWCO 30000), and the protein concentration was determined by the bicinchoninate (BCA) method. The purification was monitored by size exclusion chromatography using a 300×4.6 mm i.d. TSK-Gel Super SW 3000 column (Tosoh Co., Japan) eluted with phosphate buffer (0.1 M, pH 6.8) at a flow rate of 0.3 ml/min. Comparison to molecular mass standards (Oriental Yeast Co., Japan) of the absorbance at 280 nm indicated that a peak at 9.1 min was consistent with the presence of the 210 kDa anti-MT1-MMP mAb-SAv. Anti-MT1-MMP mAb-SAv was obtained in a yield of 36%. Negative control IgG-SAv was synthesized by the same procedure as described above in 62% yield.

Radioiodination of Biotin (3-[$^{123/125}$I]Iodobenzoyl)norbiotinamide ($^{123/125}$I-IBB) was synthesized according to the synthetic procedure outlined by Foulon *et al.*[19] with some modifications. Briefly, to a vial containing *N*-succinimidyl 3-(tributylstannyl)benzoate (72.2 μl, 2 mg/ml in methanol (1% acetic acid)) were added *N*-chlorosuccinimide (19.8 μl, 0.5 mg/ml in methanol) and concentrated $NH_4{}^{123}I$ (1110 MBq) or $Na^{125}I$ (37 MBq). The vial was vortexed, and the reaction was allowed to proceed for 30 min at room temperature. The reaction was quenched by the addition of $NaHSO_3$ (3.2 μl, 0.72 mg/ml in water), the solvent was evaporated under a stream of nitrogen, and the residue was used directly for the next reaction. A solution of norbiotinamine·HCl (Molecular Probes, Inc.) (100 μl, 3 mg/ml in *N*,*N*-dimethylformamide : water=4 : 1, pH 8.5—9.0) was added to a vial containing the $^{123/125}$I-*N*-succinimidyl 3-iodobenzoate ($^{123/125}$I-SIB) synthesized above, and the reaction was incubated for 2 h at room temperature. The product was purified by reverse-phase high-performance liquid chromatography (HPLC) using a Cosmosil $5C_{18}$-AR-300 Packed Column, 150×4.6 mm i.d. (Nacalai Tesque, Inc., Kyoto, Japan), eluting with acetonitrile : water=25 : 75 at a flow rate of 1.0 ml/min (retention time was 18 min for $^{123/125}$I-IBB). The radiochemical purity was determined by thin-layer chromatography on a silica gel plate with chloroform : methanol=6 : 1 (Rf=0.53) as eluent and by analytical HPLC under the same conditions as above. $^{123/125}$I-IBB was obtained in a radiochemical yield of 21% and 39% and a radiochemical purity of more than 94% and 95%, respectively.

Synthesis of ^{125}I Labeled Anti-MT1-MMP mAb-SAv Conjugation of ^{125}I-SIB with streptavidin was performed according to the procedure of Zalutsky and Narula[20] with slight modifications as follows: a solution of streptavidin (300 μl, 20 mg/ml in 0.15 M borate buffer (pH 8.5)) was

added to the dried residue of crude ^{125}I-SIB (32.6 MBq). After gentle agitation for 30 min at room temperature, the radioiodinated streptavidin was applied to a diafiltration membrane to remove unbound ^{125}I-SIB as well as to change buffer to PBS (0.1 M, pH 7.4). To a vial containing purified ^{125}I-streptavidin (18.5 MBq, 2.6 ml, 1.1 mg/ml in PBS), a solution of MT1-MMP mAb-Bt (1.0 ml, 3.6 mg/ml in PBS) was added, and the reaction was incubated for 1 h at room temperature followed by purification twice by affinity chromatography using a HiTrap rProtein A column. The eluate containing ^{125}I-SAv-anti-MT1-MMP mAb was concentrated with a diafiltration membrane. The protein concentration was determined by the BCA method. ^{125}I-SAv-anti-MT1-MMP mAb was obtained in a radiochemical yield of 11% and a radiochemical purity of more than 94%.

***In Vivo* Biodistribution Study** Mice were divided into 4 groups (n=3—9) for 4 or 5 time points with approximately equal distribution of tumor sizes on the day before the study. Animals were fasted for 6 h before administration of the radiopharmaceutical. Outline of the each biodistribution study is shown in Fig. 1.

One, 6, 24, 48, and 72 h after the injection of ^{125}I-SAv-anti-MT1-MMP mAb (90 kBq, 50 μg/100 μl in saline), the blood, heart, lung, liver, kidney, intestine, pancreas, spleen, muscle, brain, and tumor were excised, weighed, and counted for radioactivity with a NaI well-type scintillation counter (1470WIZARD, PerkinElmer Japan Co.) using the injected dose as a standard. Data were calculated as % injected dose (ID)/g of tissue and %ID/organ.

In the pre-targeting, ^{125}I-IBB (110 kBq, 100 μl in saline) was injected intravenously into mice 72 h after pre-treatment with anti-MT1-MMP mAb-SAv (50 μg/100 μl in saline). One, 3, 6, and 24 h after the injection of ^{125}I-IBB, the biodistribution was evaluated as described above. The biodistribution of ^{125}I-IBB alone and ^{125}I-IBB pre-targeted with negative control IgG-SAv (50 μg/100 μl in saline) were also evaluated 1, 3, 6, and 24 h post-injection in the same manner.

***In Vivo* Imaging Studies** The SPECT studies were performed using a SPECT-2000H-40 gamma camera (Hitachi Medical Co.). Mice (n=2) bearing an FM3A tumor in the right thigh received anti-MT1-MMP mAb-SAv (50 μg/100 μl in saline) *via* the tail vein. Three days later, ^{123}I-IBB (62.9 MBq/100 μL in saline) was injected followed by data acquisition as static SPECT scans (360° rotation, 30 s/step for 64 steps) using low-energy high-resolution, parallel-hole collimators (30% window, 159 keV energy peak, 128×128 matrix mode, pixel size of 2.0 mm) at 3, 6, and 24 h post injection under halothan (1.5%) anesthesia. Images were reconstructed with a standard filtered back projection algorithm.

After the SPECT scans, X-ray images of the mice were obtained for an anatomical comparison using an R-mCT system (Rigaku Co.) equipped with a fixed microfocus X-ray tube and X-ray sensor. This instrument exposes a cone-shaped X-ray beam on the 2D detector through the animal set on a stage. The revolving arm rotates 360° around the mouse for 17 s to acquire a full 3D computerized tomography (CT) data set.

Statistical Analysis To compare the time courses of radioactivity in the tumor, tumor to blood (T/B) and tumor to muscle (T/M) ratios among anti-MT1-MMP mAb-SAv pre-targeted ^{125}I-IBB, negative control IgG-SAv pre-targeted ^{125}I-IBB and ^{125}I-IBB alone, two-way factorial ANOVA followed by a Tukey–Kramer test was performed. Differences at the 95% confidence level (p<0.05) were considered significant.

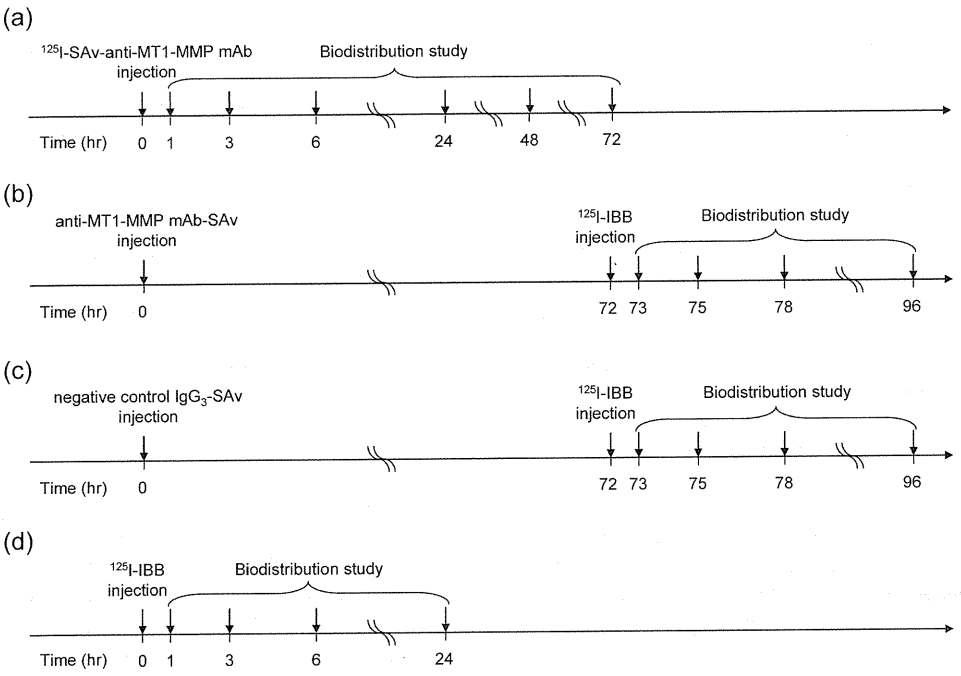

Fig. 1. Outline of the Biodistribution Studies

(a) ^{125}I-SAv-anti-MT1-MMP mAb, (b) ^{125}I-IBB pre-targeted with anti-MT1-MMP mAb-SAv, (c) ^{125}I-IBB pre-targeted with negative control IgG_3-SAv, and (d) ^{125}I-IBB alone. In each time point, biodistribution studies were conducted.

Table 1. Biodistribution of Radioactivity after the Injection of ^{125}I-SAv-anti-MT1-MMP mAb in C3H/He Mice Bearing FM3A Mouse Breast Tumors[a)]

	Time after injection (h)				
	1 (n=3)	6 (n=3)	24 (n=4)	48 (n=3)	72 (n=4)
Blood	40.65±0.44	25.29±2.47	11.93±0.88	7.27±0.35	5.62±0.51
Heart	5.71±1.31	4.58±0.42	2.88±0.38	2.10±0.06	2.04±0.36
Lung	18.35±4.28	11.88±1.71	6.36±1.16	6.63±4.06	3.55±0.68
Liver	9.36±0.43	9.32±1.23	5.89±0.34	5.70±0.54	5.63±0.67
Kidney	7.39±0.77	7.77±1.07	8.71±0.68	9.59±0.36	10.56±0.69
Intestine	1.85±0.05	2.90±0.34	1.59±0.19	1.04±0.10	0.92±0.06
Pancreas	1.12±0.17	1.44±0.30	1.22±0.14	1.02±0.08	1.23±0.12
Spleen	30.05±9.46	23.20±1.73	16.89±0.67	13.47±2.11	12.70±1.62
Muscle	0.58±0.13	0.59±0.10	0.84±0.16	0.63±0.10	0.74±0.13
Brain	0.71±0.04	0.53±0.12	0.22±0.03	0.18±0.02	0.14±0.01
Tumor	2.81±0.45	5.47±0.81	7.69±0.42	6.34±0.65	5.78±0.94
Tumor/blood	0.07±0.01	0.22±0.05	0.65±0.05	0.88±0.11	1.03±0.13
Tumor/muscle	5.16±2.11	9.48±2.44	9.44±1.78	10.31±2.22	7.87±0.26
Stomach[b)]	0.16±0.03	0.35±0.05	0.29±0.02	0.21±0.05	0.16±0.09
Urine[b,c)]			7.99±3.92	34.09±8.49	38.23±9.28
Feces[b,c)]			1.58±1.60	11.79±3.25	12.41±3.23

a) Tissue radioactivity is expressed as % injected dose per gram. Each value represents the mean±S.D. for three (1, 6, 48 h) and four (24, 72 h) animals. *b*) Expressed as % injected dose. *c*) Calculated using summated radioactivity of four animals (72 h group).

RESULTS

Immunoreactivity of Biotinylated Anti-MT1-MMP mAb The number of conjugated biotins per antibody was 2.2±0.5 when the reaction ratio of anti-MT1-MMP mAb and biotin was 1 : 12. The indices of immunoreactivity evaluated by the flow cytometry analyses were 5.8±0.9 and 6.1±1.0 for the biotinylated anti-MT1-MMP mAb and the intact anti-MT1-MMP mAb, respectively. The immunoreactivity of the anti-MT1-MMP mAb was not affected by the introduction of biotins into the anti-MT1-MMP mAb (greater than 90% retained).

Biodistribution Studies To determine the timing for post-administration, a biodistribution study of ^{125}I-SAv-anti-MT1-MMP mAb was performed first (Table 1). Radioactivity in the tumor reached a peak at 24 h (7.69% ID/g) and gradually decreased (6.34% ID/g at 48 h and 5.78% ID/g at 72 h). The kidney and spleen showed rather high radioactivity over time (10.56, 12.70% ID/g at 72 h, respectively). The T/B ratios increased in a time-dependent manner and reached greater than 1.0 at 72 h after injection. Therefore, taking into consideration radioactivity in the tumor and T/B ratios, an interval of 72 h was selected for the subsequent pre-targeting study.

Results of *in vivo* biodistribution studies of ^{125}I-IBB with pre-targeting using the anti-MT1-MMP mAb-SAv or negative control IgG-SAv are summarized in Tables 2 and 3. In the pre-targeting study targeting MT1-MMP (Table 2), ^{125}I-IBB was highly accumulated in the tumor at 3 h (2.36% ID/g) and a high level was maintained for 24 h after the injection (1.06% ID/g at 24 h) while blood clearance was rapid (0.47, 0.07% ID/g at 3, 24 h, respectively), resulting in high T/B ratios of ^{125}I-IBB early after the injection (2.55 at 1 h, 5.36 at 3 h, 7.78 at 6 h, 14.13 at 24 h). T/M ratios increased in a similar manner (3.09 at 1 h, 6.14 at 3 h, 6.99 at 6 h, 12.09 at 24 h). Other organs with the exception of the kidneys, intestine and spleen showed low radioactivity 24 h after the injection.

Radioactivity in the tumor was significantly lower (0.66% ID/g at 24 h) in the control pre-targeting study (Table 3) than in the actual pre-targeting study ($p<0.0005$), and the blood clearance was slightly slower (0.08% ID/g at 24 h). T/B ratios were significantly higher with the true pre-targeting method as compared to the control pre-targeting method ($p<0.0001$) (Fig. 2). T/M ratios were also higher with the true pre-targeting method, although these values were not significantly different between the groups. The biodistribution to other tissues, including the kidneys, intestine, spleen and liver, was similar between the groups.

In the biodistribution study of ^{125}I-IBB alone (Table 4), negligible accumulation in the tumor (0.15, <0.01% ID/g at 3, 24 h, respectively) and an extremely rapid blood clearance (0.33, 0.03% ID/g at 3, 24 h, respectively) were observed. T/B and T/M ratios were small over time (0.44, 0.58 at 1 h,

Table 2. Biodistribution of Radioactivity after the Injection of ^{125}I-IBB in C3H/He Mice Bearing FM3A Mouse Breast Tumors, Pre-targeted with Anti-MT1-MMP mAb-SAv[a)]

	Time after injection (h)			
	1 (n=9)	3 (n=8)	6 (n=9)	24 (n=9)
Blood	0.87±0.12	0.47±0.12	0.26±0.08	0.07±0.02
Heart	1.26±0.12	0.75±0.08	0.49±0.06	0.16±0.04
Lung	1.61±0.19	0.98±0.24	0.55±0.10	0.14±0.05
Liver	8.11±1.20	4.35±0.51	3.31±0.49	0.92±0.33
Kidney	73.74±6.56	62.82±11.40	45.98±6.85	20.99±3.47
Intestine	19.33±2.11	23.54±4.99	24.78±5.19	2.21±1.37
Pancreas	1.78±0.54	0.89±0.17	0.62±0.10	0.15±0.03
Spleen	9.74±2.16	8.25±1.23	6.37±2.13	2.09±1.56
Muscle	0.76±0.16	0.39±0.07	0.28±0.06	0.09±0.02
Brain	0.04±0.03	0.02±0.00	0.01±0.00	0.00±0.00
Tumor	2.22±0.58	2.36±0.78	1.89±0.27	1.06±0.39
Tumor/blood	2.55±0.52	5.36±2.49	7.78±1.79	14.13±3.51
Tumor/muscle	3.09±1.27	6.14±2.02	6.99±1.42	12.09±5.95
Stomach[b)]	0.79±0.39	0.50±0.24	0.29±0.11	0.14±0.10
Urine[b)]				23.02±10.16
Feces[b)]				18.15±4.01

a) Tissue radioactivity is expressed as % injected dose per gram. Each value represents the mean±S.D. for three (6, 24 h) and four (1, 3 h) animals. *b*) Expressed as % injected dose.

Table 3. Biodistribution of Radioactivity after the Injection of ^{125}I-IBB in C3H/He Mice Bearing FM3A Mouse Breast Tumors, Pre-targeted with Negative Control IgG-SAv[a)]

	Time after injection (h)			
	1 (n=6)	3 (n=4)	6 (n=5)	24 (n=6)
Blood	1.04±0.05	0.58±0.01	0.34±0.06	0.08±0.01
Heart	1.16±0.11	0.74±0.06	0.56±0.08	0.15±0.03
Lung	2.13±0.34	1.27±0.17	0.84±0.16	0.17±0.03
Liver	7.61±1.25	4.79±0.59	3.69±0.62	1.26±0.37
Kidney	60.71±10.23	52.12±5.09	41.26±5.34	12.87±2.15
Intestine	13.37±1.85	18.35±1.73	22.72±2.50	2.12±1.21
Pancreas	1.32±0.11	0.78±0.08	0.57±0.06	0.13±0.05
Spleen	10.89±1.65	9.82±1.37	8.07±1.91	4.32±1.28
Muscle	0.64±0.04	0.34±0.08	0.29±0.06	0.10±0.02
Brain	0.03±0.00	0.02±0.00	0.01±0.00	0.00±0.00
Tumor	1.75±0.23	1.63±0.32	1.43±0.45	0.66±0.08
Tumor/blood	1.68±0.20	2.84±0.59	4.19±0.59	8.80±0.70
Tumor/muscle	2.75±0.36	4.91±1.24	4.95±1.29	7.17±1.60
Stomach[b)]	0.30±0.08	2.42±1.96	1.20±1.20	0.45±0.65
Urine[b)]				11.95±9.27
Feces[b)]				18.59±7.93

a) Tissue radioactivity is expressed as % injected dose per gram. Each value represents the mean±S.D. for four (3 h), five (6 h) and six (1, 24 h) animals. *b*) Expressed as % injected dose.

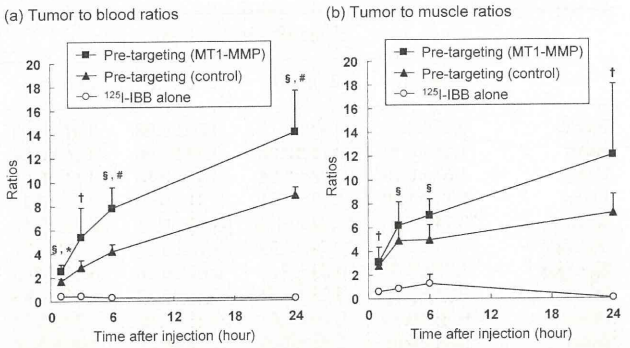

Fig. 2. (a) Tumor to Blood Ratios and (b) Tumor to Muscle Ratios of Radioactivity after the Administration of ^{125}I-IBB (Open Circle), ^{125}I-IBB Following Anti-MT1-MMP mAb-SAv (Closed Square) and ^{125}I-IBB Following Negative Control IgG-SAv (Closed Triangle)

Data are presented as the mean±S.D. Comparisons among groups were performed by two-way factorial ANOVA followed by a Tukey–Kramer test. * $p<0.05$, # $p<0.01$ *vs.* ^{125}I-IBB following negative control IgG-SAv and † $p<0.05$, § $p<0.01$ *vs.* ^{125}I-IBB.

0.42, 0.82 at 3 h, 0.30, 1.29 at 6 h, 0.16, 0.05 at 24 h, respectively). ^{125}I-IBB mainly accumulated in the intestine, followed by the kidneys and liver shortly after injection.

Imaging Studies Figure 3 shows X-ray CT (a) and SPECT images at 3 (b), 6 (c) and 24 (d) h after injection of ^{123}I-IBB in FM3A-implanted mice pre-targeted with anti-MT1-MMP mAb-SAv. The location of each tissue in the SPECT images is referenced to the X-ray CT image. The tumor was clearly visualized at 3 h after administration of ^{123}I-IBB and the accumulation of radioactivity in the tumor was maintained for 24 h. Though the kidneys, bladder and intestine were also visualized, the radioactivity in these tissues decreased relatively quickly over time compared with that in the tumor. Chest organs such as the lungs and heart, and the liver were not visualized. The distribution of signals in each tissue was very consistent with the distribution of radioactivity observed in the *in vivo* biodistribution study (Table 2).

Table 4. Biodistribution of Radioactivity after the Injection of ^{125}I-IBB in C3H/He Mice Bearing FM3A Mouse Breast Tumors[a)]

	Time after injection (h)			
	1 (n=4)	3 (n=4)	6 (n=3)	24 (n=3)
Blood	1.17±0.48	0.33±0.01	0.15±0.00	0.03±0.00
Heart	1.37±0.25	0.29±0.06	0.07±0.06	0.03±0.02
Lung	1.24±0.10	0.32±0.04	0.11±0.02	0.02±0.00
Liver	6.07±1.81	1.34±0.26	0.20±0.03	0.03±0.01
Kidney	5.61±0.84	1.02±0.20	0.42±0.21	0.08±0.01
Intestine	35.09±7.01	22.79±10.63	10.20±6.90	1.34±0.49
Pancreas	1.26±0.44	0.34±0.12	0.05±0.01	0.00±0.02
Spleen	0.56±0.07	0.13±0.05	0.04±0.04	0.02±0.04
Muscle	0.85±0.21	0.18±0.08	0.04±0.02	0.04±0.03
Brain	0.03±0.01	0.01±0.01	0.00±0.00	0.00±0.00
Tumor	0.50±0.13	0.14±0.04	0.04±0.00	0.00±0.00
Tumor/blood	0.44±0.09	0.42±0.10	0.30±0.03	0.16±0.14
Tumor/muscle	0.58±0.06	0.82±0.18	1.29±0.74	0.05±0.04
Stomach[b)]	4.03±1.27	1.17±0.82	0.24±0.18	0.37±0.35

a) Tissue radioactivity is expressed as % injected dose per gram. Each value represents the mean±S.D. for three (6, 24 h) and four (1, 3 h) animals. *b*) Expressed as % injected dose.

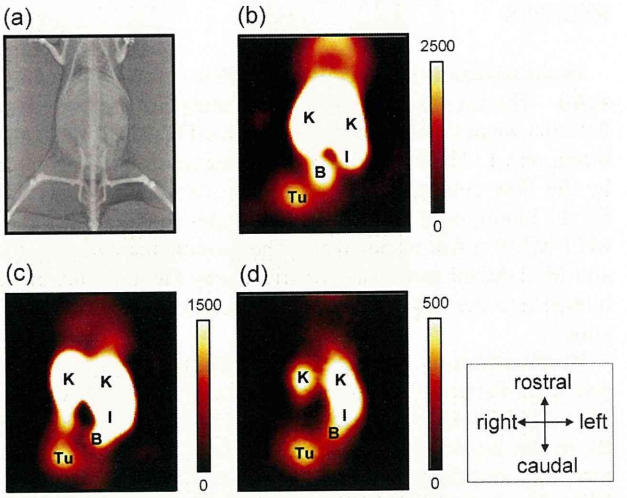

Fig. 3. X-Ray CT (a) and SPECT Images (b—d) in the Coronal Plane at 3, 6, and 24 h after the Injection of ^{123}I-IBB Pre-targeted with Anti-MT1-MMP mAb-SAv in a C3H/He Mouse Bearing an FM3A Mouse Breast Tumor

Photographs (b—d) are slices at the level of tumor and kidneys. Tu, K, I, and B indicate the tumor, kidney, intestine and bladder, respectively. SPECT images clearly visualize the tumor in the right thigh.

DISCUSSION

In this study, we developed a novel MT1-MMP imaging method based on anti-MT1-MMP mAb combined with a pre-targeting strategy using a biotin–streptavidin system. The effectiveness of this pre-targeting method (streptavidinylated anti-MT1-MMP mAb and $^{123/125}$I-IBB) was validated since significantly higher T/B ratios were achieved during the first hours after administration than had been observed in our previous study using a directly labeled antibody,[8)] and SPECT imaging clearly visualized tumor tissues *in vivo*. It should be emphasized that *in vivo* imaging of MT1-MMP relevant to the malignancy of tumors was achieved in this study.

Radiolabeled antibodies typically have a low rate of blood clearance, which can be a crucial pitfall for radioimmunodetection and radioimmunotherapy. To solve this problem, antibody fragments (Fab, scFv) and engineered variants (diabodies, triabodies, minibodies) have been investigated.[21] However, these techniques can cause problems such as reduced immunoreactivity of antibody derivatives and reduced delivery of radioactivity to the targeted organs.[22] On the other hand, the pre-targeting method has been investigated extensively, especially in tumor treatment, because of the selective accumulation of radioactivity to the targeted organ without a loss of antibody immunoreactivity and the high S/N ratio that can be achieved during the first hours after administration.[9] In fact, the introduction of a few biotins did not affect the immunoreactivity, and sulfo-NHS-LC-biotin with a spacer arm of 22.4 Å was used to minimize the steric effect by streptavidin. Recently, other reports have also shown that a pre-targeting method was effective for *in vivo* imaging of biofunctional molecules such as CD20.[11] Therefore, the pre-targeting method seems to address many of the limitations of the direct radioimaging agent approach.

In this paper, accumulated radioactivity in the tumor and T/B ratios were significantly higher in the true pre-targeting study than in the negative control pre-targeting study (ANOVA test). Thus, the accumulation of radioactivity in tumors pre-targeted with anti-MT1-MMP mAb-SAv suggests that specificity for MT1-MMP is responsible for this effect. Moreover, the tumor accumulation of ^{125}I-IBB in the absence of pre-targeting was not observed, which suggests the tumor accumulation of ^{125}I-IBB in the pre-targeting study depended on the pre-targeting antibody. As a result of rapid clearance of ^{125}I-IBB, the pre-targeting method achieved high T/B ratios significantly earlier than did our previously studied directly labeled anti-MT1-MMP mAb.[8] The T/B ratio obtained within 1 h with the pre-targeting method was higher than that from the directly labeled anti-MT1-MMP mAb at 48 h. Furthermore, tumor to lung and tumor to heart ratios from the pre-targeting method were 10.6 and 4.5 fold higher compared with the directly labeled anti-MT1-MMP mAb at 1 h after the injection of the radiolabeled probe. These results indicate the pre-targeting method provides clearer imaging of MT1-MMP in breast tumors during the first hours after administration.

Specific accumulation for MT1-MMP can be estimated by comparing the radioactivity in the tumor and T/B ratios in the true pre-targeting method with those in the negative control method. About 30—40% specific accumulation was achieved in this study, although ^{125}I-IBB accumulated in the tumor to some extent in the negative control pre-targeting study unexpectedly. This is probably caused in part by passive accumulation of the streptavidinylated antibody as a macromolecule, that is enhanced permeability and retention effect.[23] In addition, an RYD sequence contained in SAv,[24] homologous to the RGD domain, might interact with integrins expressed on the cell surface of tumors.[25] By replacing SAv with neutravidin, which lacks the RYD domain, a more specific imaging of MT1-MMP may be achieved in the future.

In the SPECT imaging study of the pre-targeting method, tumors were clearly visualized. High levels of radioactivity were also observed in the kidneys and intestine. This may be due to the high kidney uptake of pre-targeted streptavidinylated anti-MT1-MMP mAb that is dependent on the biodistribution of streptavidin itself[26] and to physiological ^{125}I-IBB accumulation in the intestine. ^{125}I-IBB also accumulated in the bladder because its molecular weight leads to glomeruli filtration. It should be stressed that chest organs such as the lungs and heart, and the liver were not visualized, which indicates the potential of this method for adequate imaging of breast tumors expressing MT1-MMP. In addition, preliminary Western blotting analysis using lysates from human breast cancer cells (MDA-MB-231) detected a high level of human MT1-MMP expression,[8] suggesting that this method may be useful in a clinical setting. We are currently investigating the effectiveness of this pre-targeting method across a variety of tumor cells that differently express MT1-MMP.

In this study, $^{123/125}$I-labeled biotin was used to demonstrate the availability of pre-targeting method for MT1-MMP because its stability, affinity to avidin and biodistribution was well examined.[19] On the other hand, ^{99m}Tc generated by a ^{99}Mo/^{99m}Tc generator on site at any time on demand is attractive for clinical use, and ^{99m}Tc-biotin may also deserve investigation on pre-targeting methods.

Biodistribution of streptavidinylated anti-MT1-MMP antibody was examined for 1—72 h. T/B ratios increased in a time dependent manner and were highest at 72 h, which has the potential that T/B ratios may be improved at the later stage after injection, leading the high contrast images of MT1-MMP. On the other hand, sensitivity can be dependent on the absolute radioactivity of $^{123/125}$I-IBB in the tumor tissue, which is an important indicator on molecular imaging. In this study, accumulation of streptavidinylated antibody in the tumor was decreased with time, indicating that $^{123/125}$I-IBB was also predicted to show the lower tumor uptake at the later stage. Thus, by taking into consideration radioactivity in the tumor and T/B ratios, we adopted the protocol such that radiolabeled biotin was administered 72 h after pre-treatment with streptavidinylated antibodies, although further studies are needed for setting the optimal interval. To date, some reports have shown that clearing agents (*e.g.* galactosylated biotin–albumin conjugate) can readily (a few hours) remove excess streptavidinylated antibodies in the circulation *via* the liver without loss of biotin binding sites in the tumor,[27,28] thus leading to a shortening of the interval needed between administration of the streptavidinylated antibody and radiolabeled biotin. In this study, we obtained the data that accumulation of streptavidinylated anti-MT1-MMP mAb was reduced after the peak at 24 h post-injection probably because of the internalization and metabolism in the tumor cells.[29] Thus, the clearing agents may enable the administration of radiolabeled biotin at the earlier time point when streptavidinylated antibody in the tumor is highly retained. This strategy will help establish an optimal protocol for sensitive MT1-MMP imaging with an aim toward clinical application.

CONCLUSION

The results clearly demonstrate the effectiveness of the pre-targeting method for imaging MT1-MMP in breast tumors with greater sensitivity and earlier post-injection analysis in comparison with the direct-radiolabeled antibody. As

mentioned previously, the amino acid sequence of the MT1-MMP protein is highly conserved among species including mouse, rat, rabbit, and human; our results obtained in experiments using rodents and MT1-MMP probes may provide important information for clinical applications and may prove to be beneficial in the diagnosis of breast tumor malignancy in the clinical setting.

Acknowledgments This study was supported by Grants-in-Aid for Scientific Research and by the 21st Century Center of Excellence Programs at Kyoto University "Knowledge Information Infrastructure for Genome Science" from the Ministry of Education, Culture, Sports, Science and Technology, Japan. A portion of this study was conducted in conjunction with the project, "R&D of Molecular Imaging Equipment for Malignant Tumor Therapy Support," which was supported by the New Energy and Industrial Technology Development Organization (NEDO), Japan.

REFERENCES

1) Sato H., Takino T., Okada Y., Cao J., Shinagawa A., Yamamoto E., Seiki M., *Nature* (London), **370**, 61—65 (1994).
2) Deryugina E. I., Quigley J. P., *Cancer Metastasis Rev.*, **25**, 9—34 (2006).
3) Jones J. L., Glynn P., Walker R. A., *J. Pathol.*, **189**, 161—168 (1999).
4) Knauper V., Bailey L., Worley J. R., Soloway P., Patterson M. L., Murphy G., *FEBS Lett.*, **532**, 127—130 (2002).
5) Holmbeck K., Bianco P., Caterina J., Yamada S., Kromer M., Kuznetsov S. A., Mankani M., Robey P. G., Poole A. R., Pidoux I., Ward J. M., Birkedal-Hansen H., *Cell*, **99**, 81—92 (1999).
6) Zhou Z., Apte S. S., Soininen R., Cao R., Baaklini G. Y., Rauser R. W., Wang J., Cao Y., Tryggvason K., *Proc. Natl. Acad. Sci. U.S.A.*, **97**, 4052—4057 (2000).
7) Chen P. S., Zhai W. R., Zhou X. M., Zhang J. S., Zhang Y. E., Ling Y. Q., Gu Y. H., *World J. Gastroenterol.*, **7**, 647—651 (2001).
8) Temma T., Sano K., Kuge Y., Kamihashi J., Takai N., Ogawa Y., Saji H., *Biol. Pharm. Bull.*, **32**, 1272—1277 (2009).
9) Boerman O. C., van Schaijk F. G., Oyen W. J., Corstens F. H., *J. Nucl. Med.*, **44**, 400—411 (2003).
10) Kraeber-Bodere F., Rousseau C., Bodet-Milin C., Ferrer L., Faivre-Chauvet A., Campion L., Vuillez J. P., Devillers A., Chang C. H., Goldenberg D. M., Chatal J. F., Barbet J., *J. Nucl. Med.*, **47**, 247—255 (2006).
11) Goldenberg D. M., Sharkey R. M., Paganelli G., Barbet J., Chatal J. F., *J. Clin. Oncol.*, **24**, 823—834 (2006).
12) Goldenberg D. M., Rossi E. A., Sharkey R. M., McBride W. J., Chang C. H., *J. Nucl. Med.*, **49**, 158—163 (2008).
13) Green N. M., *Methods Enzymol.*, **184**, 51—67 (1990).
14) Jemal A., Siegel R., Ward E., Murray T., Xu J., Smigal C., Thun M. J., *CA Cancer J. Clin.*, **56**, 106—130 (2006).
15) Zhang Y., Wang C., Zhang Y., Sun M., *Biochem. Biophys. Res. Commun.*, **325**, 1240—1245 (2004).
16) Sato T., del Carmen Ovejero M., Hou P., Heegaard A. M., Kumegawa M., Foged N. T., Delaisse J. M., *J. Cell Sci.*, **110**, 589—596 (1997).
17) Kinoh H., Sato H., Tsunezuka Y., Takino T., Kawashima A., Okada Y., Seiki M., *J. Cell Sci.*, **109**, 953—959 (1996).
18) Ishino S., Mukai T., Kuge Y., Kume N., Ogawa M., Takai N., Kamihashi J., Shiomi M., Minami M., Kita T., Saji H., *J. Nucl. Med.*, **49**, 1677—1685 (2008).
19) Foulon C. F., Alston K. L., Zalutsky M. R., *Bioconj. Chem.*, **8**, 179—186 (1997).
20) Zalutsky M. R., Narula A. S., *Int. J. Rad. Appl. Instrum. A*, **38**, 1051—1055 (1987).
21) Behr T. M., Becker W. S., Bair H. J., Klein M. W., Stuhler C. M., Cidlinsky K. P., Wittekind C. W., Scheele J. R., Wolf F. G., *J. Nucl. Med.*, **36**, 430—441 (1995).
22) Holliger P., Hudson P. J., *Nat. Biotechnol.*, **23**, 1126—1136 (2005).
23) Iyer A. K., Khaled G., Fang J., Maeda H., *Drug Discov. Today*, **11**, 812—818 (2006).
24) Argarana C. E., Kuntz I. D., Birken S., Axel R., Cantor C. R., *Nucl. Acids Res.*, **14**, 1871—1882 (1986).
25) Ruoslahti E., Pierschbacher M. D., *Science*, **238**, 491—497 (1987).
26) Schechter B., Arnon R., Colas C., Burakova T., Wilchek M., *Kidney Int.*, **47**, 1327—1335 (1995).
27) Pantelias A., Pagel J. M., Hedin N., Saganic L., Wilbur S., Hamlin D. K., Wilbur D. S., Lin Y., Stone D., Axworthy D., Gopal A. K., Press O. W., *Blood*, **109**, 4980—4987 (2007).
28) Sharkey R. M., Karacay H., Griffiths G. L., Behr T. M., Blumenthal R. D., Mattes M. J., Hansen H. J., Goldenberg D. M., *Bioconj. Chem.*, **8**, 595—604 (1997).
29) Wang X., Ma D., Keski-Oja J., Pei D., *J. Biol. Chem.*, **279**, 9331—9336 (2004).

Eur J Nucl Med Mol Imaging (2010) 37:2093–2104
DOI 10.1007/s00259-010-1521-2

ORIGINAL ARTICLE

Imaging with radiolabelled anti-membrane type 1 matrix metalloproteinase (MT1-MMP) antibody: potentials for characterizing atherosclerotic plaques

Yuji Kuge · Nozomi Takai · Yuki Ogawa · Takashi Temma · Yan Zhao · Kantaro Nishigori · Seigo Ishino · Junko Kamihashi · Yasushi Kiyono · Masashi Shiomi · Hideo Saji

Received: 17 December 2009 / Accepted: 3 June 2010 / Published online: 13 July 2010

Abstract
Purpose Membrane type 1 matrix metalloproteinase (MT1-MMP) activates pro-MMP-2 and pro-MMP-13 to their active forms and plays important roles in the destabilization of atherosclerotic plaques. This study sought to determine the usefulness of ^{99m}Tc-labelled monoclonal antibody (mAb), recognizing MT1-MMP, for imaging atherosclerosis in a rabbit model (WHHLMI rabbits).
Methods Anti-MT1-MMP monoclonal IgG_3 and negative control IgG_3 were radiolabelled with ^{99m}Tc after derivatization with 6-hydrazinonicotinic acid (HYNIC) to yield ^{99m}Tc-MT1-MMP mAb and ^{99m}Tc-IgG_3, respectively. WHHLMI and control rabbits were injected with these radio-probes. The aorta was removed and radioactivity was measured at 24 h after the injection. Autoradiography and histological studies were performed.
Results ^{99m}Tc-MT1-MMP mAb accumulation in WHHLMI rabbit aortas was 5.4-fold higher than that of control rabbits. Regional ^{99m}Tc-MT1-MMP mAb accumulation was positively correlated with MT1-MMP expression (r=0.59, p<0.0001), while ^{99m}Tc-IgG_3 accumulation was independent of MT1-MMP expression (r=0.03, p=NS). The highest ^{99m}Tc-MT1-MMP mAb accumulation was found in atheromatous lesions (4.8±1.9, %ID×BW/mm^2×10^2), followed in decreasing order by fibroatheromatous (1.8±1.3), collagen-rich (1.6±1.0) and neointimal lesions (1.5±1.5). In contrast, ^{99m}Tc-IgG_3 accumulation was almost independent of the histological grade of lesions.
Conclusion Higher ^{99m}Tc-MT1-MMP mAb accumulation in grade IV atheroma was shown in comparison with neointimal lesions or other more stable lesions. Nuclear imaging with ^{99m}Tc-MT1-MMP mAb, in combination with CT and MRI, could provide new diagnostic imaging capabilities for detecting vulnerable plaques, although further investigations to improve target to blood ratios are strongly required.

Keywords Atherosclerosis · Imaging · Matrix metalloproteinase · Antibody · Rabbit

Y. Kuge · N. Takai · Y. Ogawa · T. Temma · K. Nishigori · S. Ishino · J. Kamihashi · Y. Kiyono · H. Saji
Department of Patho-functional Bioanalysis, Graduate School of Pharmaceutical Sciences, Kyoto University, Kyoto, Japan

Y. Kuge · Y. Zhao
Department of Tracer Kinetics & Bioanalysis, Graduate School of Medicine, Hokkaido University, Sapporo, Japan

Y. Kuge (✉)
Central Institute of Isotope Science, Hokkaido University, Kita 15 Nishi 7, Kita-ku, Sapporo 060-0815, Japan
e-mail: kuge@ric.hokudai.ac.jp

Y. Kiyono
Biomedical Imaging Research Center, University of Fukui, Fukui, Japan

M. Shiomi
Institute for Experimental Animals, Kobe University Graduate School of Medicine, Kobe, Japan

Introduction

Since the rupture of atherosclerotic plaques and subsequent thrombus formation are the major causes of ischaemic diseases, such as cerebral and myocardial infarctions [1–3],

the detection of atherosclerotic plaques at higher risk for rupture is clinically important for early selection and administration of appropriate therapy. There are several techniques for imaging atherosclerotic plaques, such as computed tomography (CT), magnetic resonance imaging (MRI), ultrasound (US) and intravascular ultrasound (IVUS). These non-invasive anatomical imaging modalities offer excellent resolution and visualize the arterial lumen or calcifications. These modalities can identify the morphological alteration of atherosclerotic plaque and play important roles in finding the patients whose lesion vulnerability needs to be further evaluated. To date, however, there are no non-invasive diagnostic tools available for routine clinical use to accurately characterize atherosclerotic plaques at higher risk of rupture. Accordingly, the development of such non-invasive tools is urgently required. Using specific radio-probes, it may be possible for nuclear imaging to characterize atherosclerotic plaques as quantitative images based on cellular and biological changes, which surpasses morphological information and may help selectively detect atherosclerotic plaques at higher risk of rupture [4, 5]. Thus, the development of radio-probes is of great concern in the clinical diagnosis of atherosclerosis.

Plaques that are prone to rupture are morphologically characterized by a thin fibrous cap overlying a large lipid core. Matrix metalloproteinases (MMPs) degrade extracellular matrix that constitutes the fibrous cap of the plaques, resulting in destabilization of atherosclerotic plaques [6–8]. Increased expression of MMP-2 and MMP-9 has been demonstrated within human atherosclerotic lesions and critically implicated in plaque rupture [7, 9, 10]. MMP-2 and MMP-9 are known to cleave native type IV, V, VII and X collagens and elastin, as well as the degradation products of collagens types I, II and III after proteolysis by collagenases, such as MMP-1 and MMP-13. Thus, MMPs are considered to be involved in plaque instability [8] and are potential targets for diagnostic imaging of atherosclerotic plaques at higher risk of rupture [11, 12]. MMPs can be divided into two groups: soluble MMPs and membrane-bound MMPs. Most soluble MMPs, including MMP-2 and MMP-9, are released from cells as zymogens and require extracellular post-translational cleavage to gain biological activity [8, 13]. A membrane-bound MMP, membrane type 1 matrix metalloproteinase (MT1-MMP or MMP-14), mediates activation of pro-MMP-2 to active MMP-2 and pro-MMP-13 to active MMP-13 on the cell surface [13–15]. In our recent animal study, co-distribution of MT1-MMP and MMP-2 was demonstrated in grade IV atheroma, indicating a possible role for MT1-MMP in destabilization of atherosclerotic plaques [16]. Expression of MT1-MMP has also been found within human atherosclerotic plaques [17, 18]. Accordingly, MT1-MMP may be an important determinant of destabilization of atherosclerotic plaques and detection of MT1-MMP expression may be useful for the assessment of atherosclerotic plaques.

Taken together, nuclear imaging of MT1-MMP could provide molecular and cellular information concerning the destabilization of atherosclerotic plaques. Thus, we designed and prepared ^{99m}Tc-labelled anti-MT1-MMP monoclonal IgG (^{99m}Tc-MT1-MMP mAb) as a radio-probe for imaging atherosclerosis. Using an atherosclerosis model (myocardial infarction-prone Watanabe heritable hyperlipidaemic rabbits, WHHLMI rabbits) [19], we investigated accumulation of ^{99m}Tc-MT1-MMP mAb in atherosclerotic lesions in comparison with histological characteristics. From the data, the potential of ^{99m}Tc-MT1-MMP mAb for imaging atherosclerosis was evaluated.

Materials and methods

Design and preparation of ^{99m}Tc-MT1-MMP mAb

A purified mouse monoclonal antibody (mAb) to an oligopeptide (residues 319 to 333, numbered from the signal peptide) on human MT1-MMP (113-5B7, mouse IgG3, Daiichi Fine Chemical Co., Ltd., Toyama, Japan) [14] was used. For the control study, negative control mouse IgG_3 (ab18392, Abcam, Cambridge, UK) was used.

The anti-MT1-MMP monoclonal IgG_3 (MT1-MMP mAb) and negative control IgG_3 (IgG_3) were radiolabelled with ^{99m}Tc (^{99m}Tc-MT1-MMP mAb and ^{99m}Tc-IgG_3, respectively) after derivatization with 6-hydrazinonicotinic acid (HYNIC), according to the procedures reported previously [20–22] with slight modifications. Briefly, HYNIC-*N*-hydroxysuccinimide (NHS) was reacted with MT1-MMP mAb and IgG_3 to obtain precursors for radiolabelling (HYNIC-MT1-MMP mAb and HYNIC-IgG_3, respectively) and then purified by diafiltration. HYNIC-NHS (25 μl, 5 mg/ml) in dry *N*,*N*-dimethylformamide (DMF) was added to MT1-MMP mAb and IgG_3 solutions in 0.15 M borate buffer (pH 8.5, 2 mg/400 μl), respectively. After gentle stirring with protection from light for 2 h at room temperature, size-exclusion (SE) filtration with a diafiltration membrane [Amicon Ultra-4 (MWCO 30,000), Millipore Co., Billerica, MA, USA] using 0.01 M citrate buffer (pH 5.2) was performed to remove aggregated protein and to obtain HYNIC-MT1-MMP mAb and HYNIC-IgG_3. The purified HYNIC-MT1-MMP mAb and HYNIC-IgG_3 were stored at 4°C and used for the subsequent radiolabelling.

Radiolabelling was performed just before each experiment. To the purified HYNIC-MT1-MMP mAb and HYNIC-IgG_3 solutions (300 μg/500 μl), an equal volume of [^{99m}Tc](tricine)$_2$, prepared by the method of Larsen et al. [23], was added to obtain ^{99m}Tc-MT1-MMP mAb and

^{99m}Tc-IgG$_3$ {[^{99m}Tc](HYNIC-anti-MT1-MMP)(tricine)$_2$ and [^{99m}Tc](HYNIC-IgG$_3$)(tricine)$_2$, respectively}. After 3 h at room temperature, the radiolabelled products were purified by SE chromatography on a PD-10 desalting column (Amersham Biosciences AB, Uppsala, Sweden) using 0.05 M phosphate-buffered saline (PBS) (pH 7.0). The radiochemical purities of ^{99m}Tc-MT1-MMP mAb and ^{99m}Tc-IgG$_3$ were determined by another SE column filtration (PD-10 column) in each preparation and found to be 92.3±1.5% and 92.3±5.5%, respectively.

Animals

Three male Japanese White (JW) rabbits (3 months old, Biotek Inc., Saga, Japan) were used to obtain peritoneal macrophages. For non-invasive imaging and biodistribution studies of ^{99m}Tc-MT1-MMP mAb, four male WHHLMI rabbits (11–18 months old: 3.4±0.4 kg body weight) that were bred at Kobe University were used. Four JW rabbits (3 months old: 2.2±0.1 kg body weight, Biotek Inc., Saga, Japan) were used as controls. Four WHHLMI rabbits (two male and two female, 10–15 months old, 2.9±0.3 kg) were used for non-invasive imaging and biodistribution studies of ^{99m}Tc-IgG$_3$. The animals were fed standard chow (type CR-3, Clea Japan Inc., Tokyo, Japan) at 120 g/day and were given water ad libitum. All animal procedures were approved by the Kyoto University Animal Care Committee.

Immunoreactivity of HYNIC-MT1-MMP mAb

Rabbit peritoneal macrophages were obtained by the method of Ishii et al. [24], with minor modifications. The cells were suspended in medium A [Dulbecco's modified Eagle's medium containing 1 mM glutamine, penicillin (100 U/ml), streptomycin (100 μg/ml) and 0.2% lactalbumin hydrolysate] at a final concentration of 2.5×10^6 cells/ml. Aliquots of the cell suspension were placed into plastic Petri dishes and cultured in a humidified 5% CO_2 incubator at 37°C. After 2 h, each dish was washed twice with medium A and then cultured for a further 18 h. Cells (1×10^6 cells) were incubated with MT1-MMP mAb (50 μg/ml, 100 μl), HYNIC-MT1-MMP mAb (50 μg/ml, 100 μl) or control mouse IgG$_3$ (50 μg/ml, 100 μl) for 30 min at 4°C, followed by incubation with 10 μg/ml of Alexa Fluor® 488 goat anti-mouse IgG (100 μl, Molecular Probes, Inc., Eugene, OR, USA). For flow cytometry analysis, cells were mixed with IsoFlow solution (Beckman Coulter Inc., Fullerton, CA, USA) and immediately analysed by a FACScan instrument (Becton Dickinson Inc., Franklin Lakes, NJ, USA). Immunoreactivity of HYNIC-MT1-MMP mAb was evaluated with the median fluorescence intensity ratio to control mouse IgG$_3$ and compared with that of MT1-MMP mAb. Measurements were performed three times per rabbit using three JW rabbits.

Non-invasive imaging

After 12 h of fasting, rabbits were initially anaesthetized with ketamine (35 mg/kg, intramuscularly) and xylazine (5 mg/kg, intramuscularly). The anaesthetic state was maintained with additional doses of ketamine and xylazine during the experimental period. Rabbits were placed on the scanner bed in a prone position to include the abdominal aorta in the field of view. ^{99m}Tc-MT1-MMP mAb (140–741 MBq, 300 μg) was injected into the marginal ear vein of four WHHLMI rabbits and four control rabbits. At 10 min and 24 h after injection of the radiotracer, planar images were obtained for 10 min with a gamma camera (SPECT 2000H, Hitachi Medical Co., Tokyo, Japan) employing a low energy high resolution parallel-hole collimator with a spatial resolution of 6.7 mm in full-width at half-maximum (FWHM). Serial arterial blood samples were collected from an auricular artery. Similarly, imaging studies of ^{99m}Tc-IgG$_3$ were performed after the injection of ^{99m}Tc-IgG$_3$ (91–198 MBq, 300 μg) into the marginal ear vein of four WHHLMI rabbits. All rabbits were also applied to the biodistribution studies described below.

Biodistribution studies

Immediately after the non-invasive imaging studies, 24 h after tracer injection, the animals were sacrificed with an overdose of pentobarbital. The ascending-arch, thoracic and abdominal aortas, blood and other tissues were removed. The ascending-arch aortas were divided into six segments, while the thoracic and abdominal aortas were divided into nine segments (Fig. 1). Each segment was weighed and immediately fixed in a solution containing L-(+)-lysine hydrochloride (75 mM) and 4% paraformaldehyde in phosphate buffer (37.5 mM, pH 7.4). The radioactivity of each sample was measured with a well-type gamma counter (ARC-2000, Aloka, Tokyo, Japan). Results were expressed as the differential uptake ratio (DUR), which was calculated as (tissue activity/tissue weight)/(injected radiotracer activity/animal body weight), with activities given in becquerels and weights given in grams. The aorta to blood ratio (A/B ratio) and the aorta to muscle ratio (A/M ratio) were calculated from DUR values.

Autoradiography (ARG)

Autoradiographic studies were also performed using the aortas obtained at 24 h after tracer injection (the same aortas used in the biodistribution studies). A total of eight

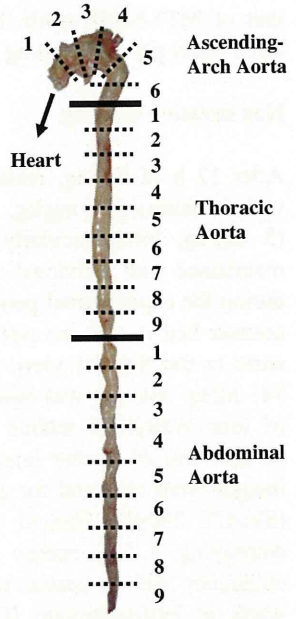

Fig. 1 Segmentation of the ascending-arch, thoracic and abdominal aortas. The ascending-arch aortas were divided into six segments, while the thoracic and abdominal aortas were divided into nine segments

segments, the second and fifth segments from the ascending-arch aorta, and the second, fifth and eighth segments from the thoracic and abdominal aortas, from each animal were used for autoradiographic studies. These segments were frozen and cut into 20-μm thick slices using a cryomicrotome. To obtain ^{99m}Tc-MT1-MMP mAb and ^{99m}Tc-IgG$_3$ autoradiograms, sections were thaw-mounted on silane-coated slides, which were then placed on a phosphor image plate (Fuji Imaging Plate BAS-UR, Fuji Photo Film, Tokyo, Japan) for 24 h together with calibrated standards ($^{99m}TcO_4^-$solution). The ARG images were analysed using a computerized imaging analysis system (Bio-Imaging Analyzer BAS2500 and Image Gauge Software, Fuji Photo Film, Tokyo, Japan). Radioactivity in each region of interest (ROI) was expressed as %ID×BW/mm^2, calculated as (radioactivity in ROI)/(injected radioactivity/animal body weight), with radioactivity in ROI given in becquerels/mm^2, injected activity given in becquerels and weight given in grams.

Histological analysis

Serial sections of ARG slices were subjected to histological analysis. Azan-Mallory staining, haematoxylin and eosin (H&E) staining and immunohistochemical staining (MT1-MMP, macrophage and smooth muscle cell) were performed. Immunohistochemical staining of MT1-MMP was carried out using the anti-MT1-MMP monoclonal IgG (MT1-MMP mAb, described above) and a Dako EnVision + kit (Dako, Tokyo, Japan) with haematoxylin counterstaining. In the same manner, immunohistochemical staining for macrophages and smooth muscle cells was carried out with a rabbit macrophage-specific mAb, RAM11 (Dako, Tokyo, Japan) and a human smooth muscle actin-specific mAb, 1A4 (Dako, Tokyo, Japan), respectively. Immunostaining with subclass-matched irrelevant IgG served as a negative control. Azan-Mallory staining and H&E staining were performed with standard procedures. Areas (μm^2) occupied by each lesion component were evaluated with a VHX Digital Microscope (Keyence Corp., Osaka, Japan). Collagen-rich fibres and extracellular lipid deposits (extracellular vacuoles and lacunae) were assessed with Azan-Mallory staining. Macrophage and smooth muscle cell areas were determined by immunohistochemical staining (RAM11 and 1A4). MT1-MMP expression density was assessed as a percentage of positively stained areas (% positive).

Classification of atherosclerotic lesions

The atherosclerotic lesions in WHHLMI rabbits were divided into four categories using a classification scheme based on the recommendations of the American Heart Association (AHA) [25, 26] by Azan-Mallory staining and H&E staining as previously described [27, 28] (Fig. 2a–p): (1) neointimal lesion (type I–III), (2) atheromatous lesion (type IV), (3) fibroatheromatous lesion (type Va, Vb) and (4) collagen-rich lesion (type Vc). Neointimal lesions were defined as having adaptive thickening of the intima consisting of mainly smooth muscle cells and few macrophages. Atheromatous lesions contained thin fibrous connective tissue and a dense accumulation of extracellular lipid and foam cells and were considered to be vulnerable-like lesions in human atherosclerotic plaques. Fibroatheromatous lesions were composed of several lipid cores, separated by thick layers of fibromuscular connective tissue, which was relatively stable to rupture [29]. Collagen-rich lesions consisted of a predominantly collagenous component and contained smooth muscle cells.

ROIs were placed to cover each atherosclerotic lesion in the aorta section of the WHHLMI rabbit and then transferred to the corresponding ARG images (Fig. 2q–v).

Statistical analysis

Data are presented as the mean ± SD. Statistical analysis was performed with the Kruskal-Wallis test with post hoc analysis by the Holm test (Table 1). Correlation coefficients were assessed by Spearman rank correlation coefficients (Fig. 4i, j). Comparisons among lesion types were performed using the Kruskal-Wallis test with post hoc analysis by the Holm test (Fig. 5a, b). A two-tailed value of $p<0.05$ was considered statistically significant.

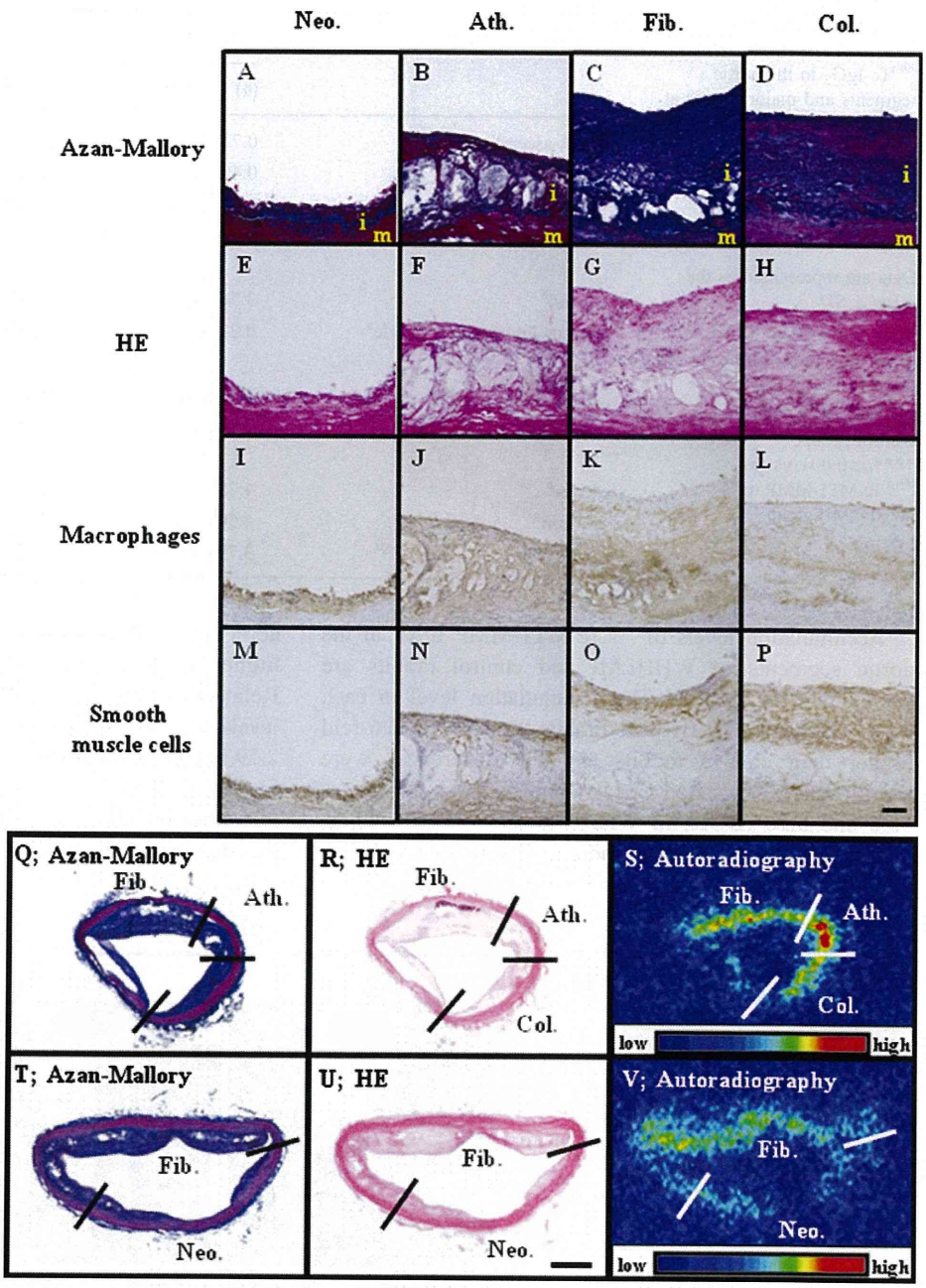

Fig. 2 Representative photomicrographs of histological features (**a–p**) and lesion classification (**q–v**) of atherosclerotic lesions in WHHLMI rabbits. Atherosclerotic lesions were microscopically divided into four categories as described in the "Materials and methods" section: neointimal lesion (*Neo.*, *left column*), atheromatous lesion (*Ath.*, *second column*), fibroatheromatous lesion (*Fib.*, *third column*) and collagen-rich lesion (*Col.*, *right column*). ROIs were placed to cover each atherosclerotic lesion in the aorta section of the WHHLMI rabbit and then transferred to the corresponding ARG images. *m* media, *i* intima, *bar* = 100 μm (**a–p**) and 1 mm (**q–v**)

Results

Immunoreactivity of HYNIC-MT1-MMP mAb

By FACS analysis, the signals of MT1-MMP mAb and HYNIC-MT1-MMP mAb were clearly distinct from that of the negative control IgG_3. The median fluorescence intensity ratios of MT1-MMP mAb and HYNIC-MT1-MMP mAb to control IgG_3 were 2.99±0.26 and 2.36±0.92, respectively, and the difference was not statistically significant (Kruskal-Wallis test).

Non-invasive imaging and biodistribution studies

Planar images showed primarily blood pool radioactivity in the abdominal aorta of every rabbit at 10 min after injection of ^{99m}Tc-MT1-MMP mAb or ^{99m}Tc-IgG_3 (Fig. 3a–c). At 24 h, the atherosclerotic abdominal aorta was clearly visible in the WHHLMI rabbits given ^{99m}Tc-MT1-MMP mAb with decreased blood pool radioactivity within the abdominal aorta (Fig. 3d–f). Relatively high ^{99m}Tc-MT1-MMP mAb accumulations were found in the liver, spleen and kidneys of both WHHLMI and control rabbits.

Table 1 Accumulation levels of ^{99m}Tc-MT1-MMP mAb and ^{99m}Tc-IgG$_3$ in the aortic segments and major organs at 24 h after injection

Segments	^{99m}Tc-MT1-MMP mAb		^{99m}Tc-IgG$_3$
	(a) Control	(b) WHHLMI	(c) WHHLMI
Arch-ascending[a]	0.75±0.37	2.96±1.07**	2.12±0.43***
Thoracic[a]	0.40±0.12	2.48±0.72**	2.03±0.64***
Abdominal[a]	0.27±0.14	1.77±0.50**	0.97±0.51****
Total[a]	0.44±0.29	2.38±0.90**	1.65±0.76****
Blood[a]	3.76±0.89	5.86±0.93*	5.72±1.08
Vastus intermedius muscle[a]	0.23±0.15	0.48±0.64	0.23±0.22
A/B ratio	0.12±0.08	0.40±0.13**	0.30±0.14****
A/M ratio	2.50±1.9	14.3±11.6**	11.0±8.1
Liver[a]	4.23[b]	2.79[b]	ND
Spleen[a]	4.50[b]	3.52[b]	ND
Kidneys[a]	3.79[b]	3.32[b]	ND

Data are represented as the mean ± SD

A/B ratio aorta to blood ratio, *A/M ratio* aorta to muscle ratio, *ND* not determined

*$p<0.05$; **$p<0.001$ vs (a) control group; ***$p<0.05$; ****$p<0.001$ vs (b) ^{99m}Tc-MT1-MMP mAb (WHHLMI) group

[a] DUR

[b] $n=1$ due to technical problems

Accumulation levels of ^{99m}Tc-MT1-MMP mAb in the aortic segments of WHHLMI and control rabbits are summarized in Table 1. The accumulation level in each aortic segment of WHHLMI rabbits was 3.9- to 6.6-fold higher than control rabbits and the differences were significant. Mean blood pool radioactivity at 24 h was 5.86 and 3.76 (DUR) in WHHLMI and control rabbits, respectively. Aorta to blood radioactivity ratios (A/B) and aorta to muscle radioactivity ratios (A/M) were significantly higher in WHHLMI rabbits than in control rabbits. Relatively high ^{99m}Tc-MT1-MMP mAb accumulation levels were detected in the liver (4.23 in WHHLMI and 2.79 in control rabbits), spleen (4.50 in WHHLMI and 3.52 in control rabbits) and kidneys (3.79 in WHHLMI and 3.32 in control rabbits) of both rabbits. No marked difference in the distribution of ^{99m}Tc-MT1-MMP mAb in non-target

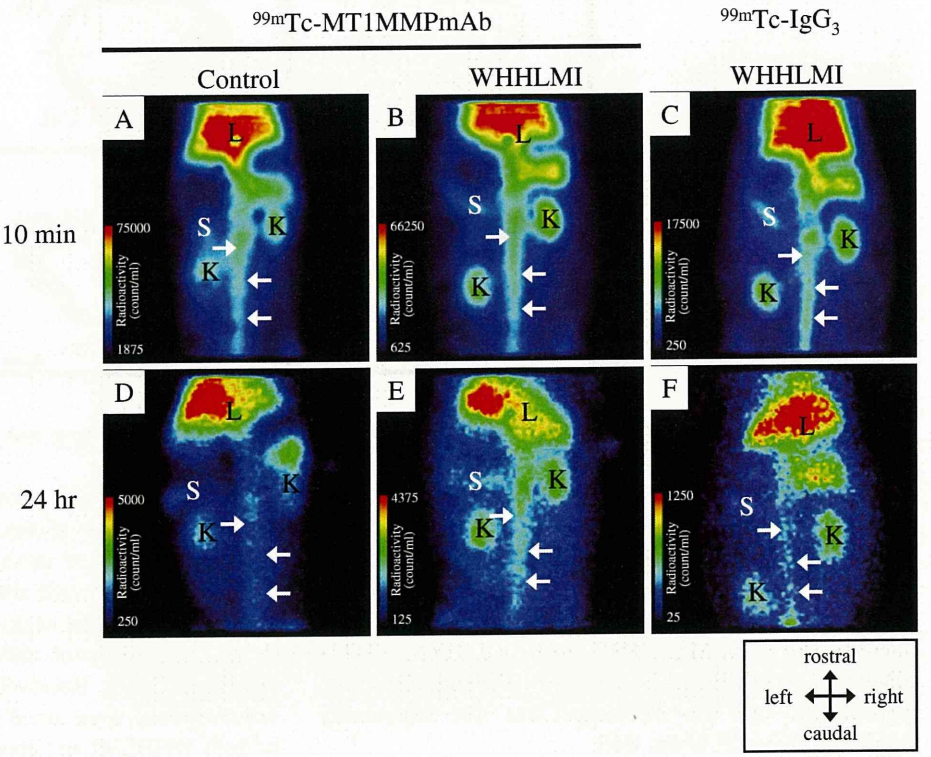

Fig. 3 Non-invasive imaging of the abdominal region with ^{99m}Tc-MT1-MMP mAb and ^{99m}Tc-IgG$_3$. Planar images for the control (**a**, **d**) and WHHLMI rabbits (**b**, **c**, **e**, **f**) at 10 min (**a**–**c**) and 24 h (**d**–**f**) after injection of ^{99m}Tc-MT1-MMP mAb (**a**, **b**, **d**, **e**) or ^{99m}Tc-IgG$_3$ (**c**, **f**). *Arrows*, *L*, *K* and *S* mark the aorta, liver, kidney and spleen, respectively

organs was observed between WHHLMI and control rabbits.

Regional distribution of ^{99m}Tc-MT1-MMP mAb in comparison with MT1-MMP expression

In the ARG study, heterogeneous ^{99m}Tc-MT1-MMP mAb accumulation was observed in the intima of WHHLMI rabbit aortas, while no marked accumulation was found in the aortas of control rabbits (Fig. 4a, b). No marked accumulation was also found in the aortas of WHHLMI rabbits given ^{99m}Tc-IgG$_3$ (Fig. 4c). MT1-MMP expression was detected in the intimal regions of the WHHLMI rabbit aorta, and the expression level was different among the regions (Fig.4e, g, h). Higher accumulation levels of ^{99m}Tc-MT1-MMP mAb were found in regions with high MT1-MMP expression, whereas lower accumulation was observed in regions with low MT1-MMP expression. No obvious MT1-MMP expression was observed in the aorta of control rabbits (Fig. 4d, f). Figure 4i, j shows the relationship of MT1-MMP expression density with ^{99m}Tc-MT1-MMP mAb accumulation and ^{99m}Tc-IgG$_3$, respectively. Regional ^{99m}Tc-MT1-MMP mAb accumulation levels in the aorta section were positively correlated with MT1-MMP expression density in WHHLMI rabbits (r=0.59, p<0.0001). On the other hand, ^{99m}Tc-IgG$_3$ accumulation was independent of MT1-MMP expression density (r=0.03, p=NS).

Relationship between ^{99m}Tc-MT1-MMP mAb accumulation and histological characteristics

Figure 2a–p shows representative photomicrographs of the histological features of each atherosclerotic lesion category in WHHLMI rabbits. The histopathological features, which correspond to the classification criteria, observed in the ascending-arch and thoracic aortas of WHHLMI rabbits were as follows: neointimal (n=15 for ^{99m}Tc-MT1-MMP mAb study and n=13 for ^{99m}Tc-IgG$_3$ study), atheromatous (n=39 and n=31, respectively), fibroatheromatous (n=36 and n=35, respectively) and collagen-rich (n=59 and n=41, respectively). No lesions showed haemorrhage, plaque rupture or thrombi (type VI) in the present study.

^{99m}Tc-MT1-MMP mAb accumulation level was dependent on the histological grade of the lesions (Fig. 5a, Table 2) and was prominently and significantly the highest (p<0.0001) in atheromatous lesions (type IV) compared with those in other lesions. Accumulation level of ^{99m}Tc-MT1-MMP mAb in atheromatous lesions was 3.3-, 2.7- and 3.0-fold higher than those in the neointimal, fibroatheromatous and collagen-rich lesions, respectively. In contrast, the ^{99m}Tc-IgG$_3$ accumulation level was markedly lower than ^{99m}Tc-MT1-MMP mAb. The ^{99m}Tc-IgG$_3$ accumulation level was independent of the histological grade of lesions, except for slightly but significantly lower ^{99m}Tc-IgG$_3$ level in the neointimal lesion (Fig. 5a, Table 2).

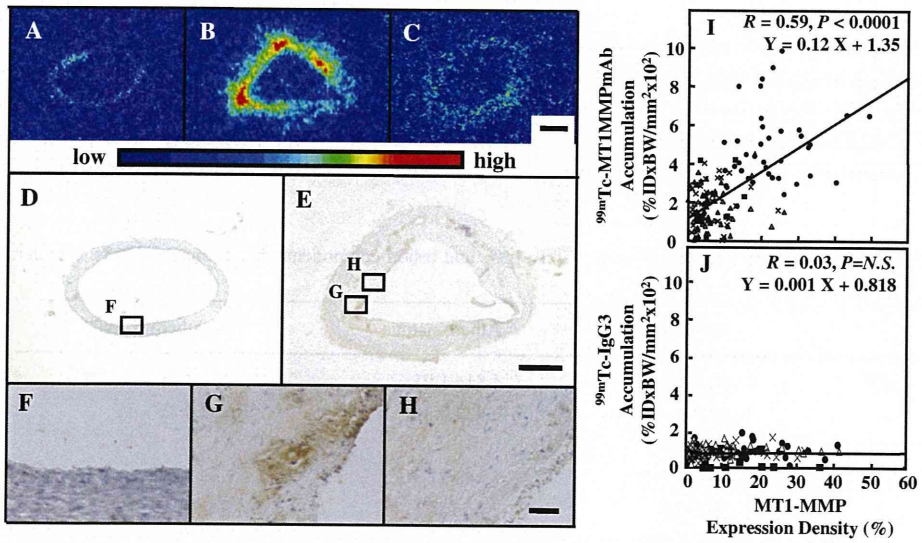

Fig. 4 Regional distribution of ^{99m}Tc-MT1-MMP mAb and ^{99m}Tc-IgG$_3$, and MT1-MMP expression in aorta sections. **a–c** Autoradiograms of ^{99m}Tc-MT1-MMP mAb in the control (**a**) and WHHLMI (**b**) rabbits and ^{99m}Tc-IgG$_3$ in a WHHLMI rabbit (**c**). **d–h** MT1-MMP immunohistochemical staining of the control (**d** and **f**) and WHHLMI rabbits (**e**, **g** and **h**). **f–h** High magnification images of MT1-MMP immunohistochemical staining in the regions depicted in **d** and **e**. Regression analyses of MT1-MMP expression density with ^{99m}Tc-MT1-MMP mAb accumulation (**i**) and ^{99m}Tc-IgG$_3$ (**j**) are shown. An identical colour window was applied to all autoradiographic images (**a–c**). *Bar* = 1 mm (**a–e**) and 100 μm (**f–h**). ■ neointimal lesion, • atheromatous lesion, x fibroatheromatous lesion, Δ collagen-rich lesion

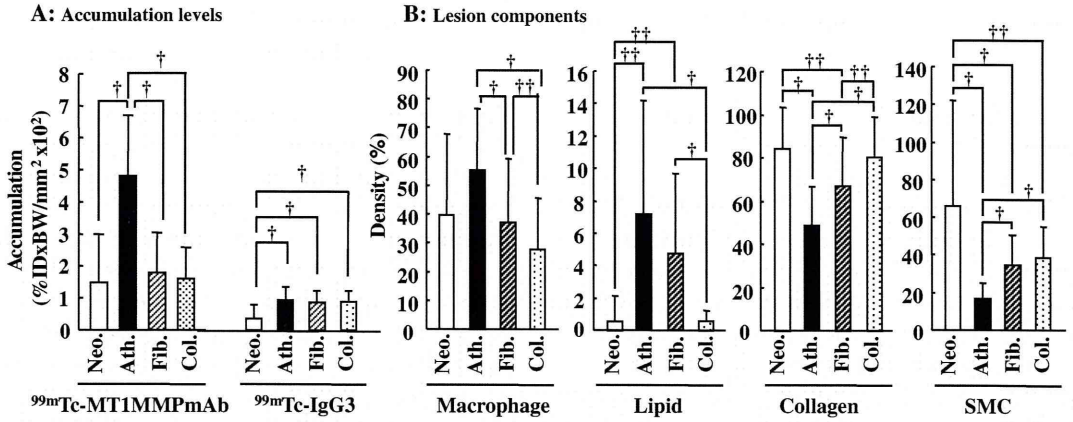

Fig. 5 Distribution profiles of ^{99m}Tc-MT1-MMP mAb, ^{99m}Tc-IgG$_3$ (**a**) and lesion components (macrophages, lipids, collagen and smooth muscle cells) (**b**) in each lesion category. *Neo.*, *Ath.*, *Fib.* and *Col.* neointimal, atheromatous, fibroatheromatous and collagen-rich lesions, respectively. *SMC* smooth muscle cells. Data are represented as the mean ± SD. †$p<0.01$; ††$p<0.05$

Figure 5b and Table 2 show the lesion components (i.e. macrophages, lipids, collagen and smooth muscle cells) quantified for each lesion category. The macrophage and lipid density was also the highest in the atheromatous lesions among the four lesion categories. Consequently, the highest level of ^{99m}Tc-MT1-MMP mAb accumulation, macrophage density and lipid density were observed in atheromatous lesions. On the other hand, the collagen and smooth muscle cell density was the lowest in atheromatous lesions among the four lesion categories.

Discussion

Aiming to develop a non-invasive means for discriminating atherosclerotic lesions at higher risk of rupture (atheromatous lesions) from more stable lesions, the potential of a radio-probe, ^{99m}Tc-MT1-MMP mAb, was evaluated in an atherosclerotic WHHLMI rabbit model. Consequently, significantly higher ^{99m}Tc-MT1-MMP mAb accumulation was found in grade IV atheroma in comparison with neointimal lesions or other more stable lesions. Thus, the potential of ^{99m}Tc-MT1-MMP mAb was demonstrated for nuclear imaging of MT1-MMP expression and selectively detecting atheromatous lesions.

Comparison with ^{99m}Tc-annexin A5 and ^{18}F-FDG

Our major interest is the prominently higher ^{99m}Tc-MT1-MMP mAb accumulation in grade IV atheroma in comparison with neointimal lesions or other more stable lesions. It will be of great importance to compare the accumulation profile of ^{99m}Tc-MT1-MMP mAb with that of ^{99m}Tc-annexin A5, a marker of ongoing apoptotic cell death, and ^{18}F-FDG, a marker of inflammation, as both ^{99m}Tc-annexin A5 and ^{18}F-FDG have been applied to clinical studies and are considered to be the most promising radio-probes for evaluation of plaque characteristics [5, 11]. Surprisingly, the accumulation

Table 2 Distribution profiles of ^{99m}Tc-MT1-MMP mAb, ^{99m}Tc-IgG$_3$ and lesion components (macrophages, lipids, collagen and smooth muscle cells) in each lesion category

	Neointimal	Atheromatous	Fibroatheromatous	Collagen-rich
^{99m}Tc-MT1-MMP mAb[a]	1.48±1.51	4.81±1.91	1.79±1.26	1.60±0.98
^{99m}Tc-IgG$_3$[a]	0.35±0.41	0.93±0.38	0.86±0.32	0.89±0.29
Macrophage[b]	39.8±27.8	55.4±21.3	37.3±22.3	27.8±17.6
Lipid[b]	1.6±2.5	7.2±7.0	4.8±4.9	0.7±0.7
Collagen[b]	84.0±18.9	48.6±18.5	66.9±22.3	80.1±18.3
SMC[b]	65.7±56.5	16.8±8.1	34.4±16.1	38.1±17.2

Data are represented as the mean ± SD. For the results of statistical analysis, see Fig. 5

[a] Accumulation (%ID×BW/mm^2 ×10^2)

[b] Density (%)

ratios of atheromatous lesions to other lesions of ^{99m}Tc-MT1-MMP mAb (**A**theromatous/**N**eointimal = 3.3, **A**theromatous/**F**ibroatheromatous = 2.7 and **A**theromatous/**C**ollagen-rich ratio = 3.0) were markedly higher than those of ^{99m}Tc-annexin A5 (**A/N**=1.3, **A/F**=1.3 and **A/C**=1.8) [28]. These results suggest the ability of ^{99m}Tc-MT1-MMP mAb to selectively detect grade IV atheroma among heterogeneous atherosclerotic lesions. On the other hand, a recent clinical study showed that vascular uptake of FDG was seen in a substantial portion (50%) of patients who had undergone FDG positron emission tomography (PET) imaging for various indications (i.e. malignant tumours, solitary pulmonary nodules or liver masses and benign diseases) [30]. Our previous study in apolipoprotein E null mice also showed relatively high ^{18}F-FDG accumulation levels in early lesions, resulting in lower accumulation ratios for advanced to early lesions in comparison with ^{99m}Tc-annexin A5 [31]. Thus, the desirable features of ^{99m}Tc-MT1-MMP mAb further confirm its potential as a radio-probe for detecting atheromatous lesions. It should be noted here that ^{18}F-FDG is considered to be the most promising probe for identifying inflamed atherosclerotic lesions. This is probably because of the higher absolute uptake levels of ^{18}F-FDG, which may be advantageous for lesion detection [28, 31, 32]. ^{18}F-FDG, as well as CT, MRI and US, can be used to find the patients whose lesion vulnerability needs to be further evaluated. The preferential uptake of ^{99m}Tc-MT1-MMP mAb in atheromatous lesions may be a useful indicator of advanced lesions, although it is still necessary to further demonstrate whether ^{99m}Tc-MT1-MMP mAb is also useful for characterizing atherosclerosis in the course of lesion development, as well as grade IV atheroma.

Immunoreactivity and specificity of ^{99m}Tc-MT1-MMP mAb

Immunoreactivity and specificity are indispensable prerequisites of in vivo nuclear imaging probes utilizing immunodetection. In this study, anti-MT1-MMP monoclonal IgG_3 (MT1-MMP mAb) was labelled with ^{99m}Tc after derivatization with HYNIC. Flow cytometry analyses indicated that modification of MT1-MMP mAb with the chelating moiety (HYNIC) does not significantly affect the immunoreactivity of the original MT1-MMP mAb. In addition, ARG and immunohistochemical studies showed that ^{99m}Tc-MT1-MMP mAb but not ^{99m}Tc-IgG_3 accumulation in atherosclerotic lesions was well correlated with MT1-MMP expression density (Fig. 4i, j). Furthermore, Fig. 5a and Table 2 confirmed the low and almost non-specific accumulation of ^{99m}Tc-IgG_3 among the lesion categories. Our previous studies also showed that accumulation of ^{99m}Tc-labelled non-specific IgG_{2a} in atheromatous lesions was not significantly different from other types of lesions (i.e. neointimal lesion, fibroatheromatous lesion, collagen-rich lesion) [33]. These findings strongly suggest the potential of ^{99m}Tc-MT1-MMP mAb to specifically recognize MT1-MMP in vivo, although experiments using radiotracers with higher radiochemical purities and further characterization of the labelled antibodies are required to confirm the present results and prove the usefulness of nuclear imaging with ^{99m}Tc-MT1-MMP mAb.

Limitations in ^{99m}Tc-MT1-MMP mAb imaging and the present study design

Another prerequisite of radio-probes is a rapid clearance of radioactivity from the blood and tissues surrounding the target lesions. One drawback of our ^{99m}Tc-MT1-MMP mAb is its relatively slow clearance from the blood, which is an intrinsic problem of radio-probes utilizing antibodies. The A/B ratio in WHHLMI rabbits was 0.40±0.13 at 24 h, indicating that the radioactivity detected in the in vivo imaging study was from both the aorta and blood. Thus, the clearance of ^{99m}Tc-MT1-MMP mAb does not match the short half-life of ^{99m}Tc. Recent advances in antibody engineering, however, should provide a promising solution to this issue. Radio-probes derived from low molecular weight polypeptides or compounds, small recombinant antibody fragments (Fab, scFv) or engineered variants (diabodies, triabodies, minibodies and single-domain antibodies) show rapid clearance of radioactivity from the circulation [34]. Pretargeting antibody methods appear to provide another solution to achieve the rapid clearance of radioactivity from the circulation [35]. Image subtraction techniques and/or kinetic model analysis, particularly those with dual isotope single photon emission computed tomography (SPECT) imaging techniques, may also help address this issue [36]. Semiconductor detector technologies contribute to separate signals from each isotope [37]. Accordingly, ^{99m}Tc-MT1-MMP mAb still appears to have the potential as an in vivo nuclear imaging probe that deserves further investigation.

Here, it should be noted that the blood level of ^{99m}Tc-MT1-MMP mAb in WHHLMI rabbits is significantly higher than that in control rabbits (Table 1). Atherosclerotic changes have been shown to be associated with hepatic and renal dysfunctions [38, 39]. Our preliminary in vitro incubation study showed that >95% of ^{99m}Tc-MT1-MMP mAb remained unchanged in rabbit plasma up to 24 h (data not shown). Accordingly, the high blood level of ^{99m}Tc-MT1-MMP mAb in WHHLMI rabbits may be caused by disturbed metabolism/excretion owing to dyshepatia or dysnephria, although the exact reason remains unclear. Our previous study on annexin A5 also showed slower blood clearance of the tracer in WHHLMI rabbits [28].

In addition to the high blood pool radioactivity, the limited spatial resolution of nuclear imaging modalities and cardiac and respiratory motion may hamper imaging of culprit lesions in moving coronary arteries. The limitation, however, may be partly solved by coregistration with CT or MRI to obtain anatomical information [11]. In this regard, PET/CT or SPECT/CT technology has gained increasing interest in the clinical imaging of atherosclerotic plaques. On the other hand, respiratory and electrocardiographic gating techniques seem to be a promising approach to solve the problem of cardiac and respiratory motion [11]. Further, SPECT imaging of small experimental animals is rapidly gaining in popularity, thanks to the development of advanced multi-pinhole collimation technologies [40]. Multi-pinhole collimation technologies may largely improve the spatial resolution of SPECT scanners, although their sensitivity is still limited. Compared with SPECT, PET has several advantages, including its higher resolution with higher sensitivity and better quantitative nature. Accordingly, the development of positron-labelled radiotracers may be another option to solve the limitation, although additional molecular design, including that for accelerating blood clearance and use of positron emitters with longer half-lives (^{64}Cu and ^{124}I), is required.

Hepatic and renal radioactivity accumulation is one of the most important concerns in nuclear imaging utilizing radiolabelled antibodies [41]. The present results showed a relatively high radioactivity accumulation in the kidneys (Table 1). It is well known that most radiolabelled mAbs show very high liver uptake due to the hepatic clearance. Unfortunately, the exact reason for the high renal accumulation remains unclear. However, it may be ascribed to the metabolic and/or degradation products of the labelled compound, as the present experiment performed at 24 h (relatively late phase) after the radiotracer injection. Low molecular weight metabolic and/or degradation products are preferentially excreted via kidneys [41]. Another explanation may be characteristics of the labelled antibody, as ^{99m}Tc-MT1-MMP mAb also showed relatively high renal accumulation in rats and mice at 1 h after the radiotracer injection [42]. Several investigators reported relatively high renal accumulation of radiolabelled mAbs [43–45]. Further studies, including in vivo metabolite analysis, would help clarify the reason for the high renal accumulation of radioactivity derived from ^{99m}Tc-MT1-MMP mAb. On the other hand, the planar images showed significantly higher radioactivity accumulation in the liver than that in the kidneys (Fig. 3). As for the discrepancy between the biodistribution and imaging studies (Table 1 and Fig. 3), the reason can be explained by the planar imaging technique used in the present study. Planar images apparently show higher radioactivity accumulation in the larger (thicker) organs, as they represent summation of radioactivity for the y-axis of the body.

MMPs as a target molecule for imaging plaques at higher risk of rupture

Macrophages secrete enzymes that degrade the fibrous cap of the plaque, including several members of MMPs [16, 46, 47]. MT1-MMP and MMP-2 expression was prominently observed in the macrophage-rich regions of the atheromatous lesions [16]. The high ^{99m}Tc-MT1-MMP mAb accumulation in grade IV atheroma found in the present study can be partly ascribed to the accumulated macrophages in the lesion as shown in Fig. 5 and Table 2. For nuclear imaging of MMPs, several broad-spectrum MMP inhibitors (MPI), including HO-CGS 27023A, have been radiolabelled [11, 12, 48]. Experimental studies in apolipoprotein E null mice indicated that ^{123}I-HO-CGS 27023A could specifically image MMP activity by scintigraphy of MMP-rich vascular lesions in vivo [49]. Another MPI, labelled with ^{111}In (RP780), has been used to image atherosclerotic lesions in a rabbit model [11, 12, 50]. A significantly higher level of immunostaining for MMPs was observed in plaque segments demonstrating higher accumulation of the ^{111}In-labelled MPI. Zhang et al. [51] also showed the potentials of ^{111}In-labelled MPI (RP782), which binds to the activated catalytic domain of MMPs, for detecting injury-induced vascular remodelling in apolipoprotein E null mice. Recently, Fujimoto et al. reported on ^{99m}Tc-labelled MPI (RP805) [52]. On the other hand, Lancelot et al. [53] demonstrated the usefulness of MMPs as a target for the characterization of atherosclerotic lesions, by using a gadolinium (Gd)-based MRI contrast agent that targets MMPs (P947, Gd-labelled MPI). These findings support the present results and indicate the potential of MMPs as a suitable target for in vivo imaging of atherosclerosis. Here, it should be noted that these radiolabelled broad-spectrum MPIs mainly recognize soluble MMPs, including MMP-2, -8, -9 and -13, while our ^{99m}Tc-MT1-MMP mAb recognizes a membrane-bound MMP, MT1-MMP (MMP-14). It may be advantageous to utilize membrane-bound MMPs as a target molecule for imaging because most soluble MMPs are released from cells, which may result in diffuse distribution of the enzymes and elevated circulating MMP levels, and may cause elevated background levels during in vivo imaging. Conversely, it remains unclear and should be clarified which MMP subtype is the most suitable target for in vivo imaging and whether specific or broad-spectrum imaging of MMPs is more useful for determining plaques at higher risk of rupture.

It is very important to discuss the potentials of target molecules other than MMPs. Our previous study in WHHLMI rabbits showed the co-distribution of MT1-

MMP, MMP-2 and cyclooxygenase 2 (COX-2) in grade IV atheroma, indicating a possible link among these enzymes in the destabilization of atherosclerotic plaques [16]. Relatively high COX-2 expression levels, however, were also observed in other more stable lesions, indicating that COX-2 is less suitable for determining plaques at higher risk of rupture. We also evaluated the potentials of lectin-like oxidized low-density lipoprotein (LDL) receptor 1 (LOX-1), a cell surface receptor for oxidized LDL, as a target molecule for determining plaques at higher risk of rupture [33]. Consequently, the accumulation ratios of ^{99m}Tc-labelled anti-LOX-1 mAb for atheromatous lesions to other lesions (**A/N** = 2.7, **A/F** = 1.9 and **A/C** lesion ratios = 2.4) were higher than those of ^{99m}Tc-annexin A5 but less than those of ^{99m}Tc-MT1-MMP mAb. These findings further confirmed the potentials of MT1-MMP as a target molecule for determining plaques at higher risk of rupture. On the other hand, several promising atherosclerosis-targeted imaging agents, including those for macrophage activity, angiogenesis, apoptosis and cell tracking, have been reported [5]. Extensive studies are now ongoing to prove which target molecule is more suitable for characterizing the vulnerability of atherosclerotic plaques and for identifying patients at higher risk of cardiovascular events [5]. Our series of studies in WHHLMI rabbits [28, 33] and apolipoprotein E null mice [31] using ^{18}F-FDG, ^{99m}Tc-annexin A5, ^{99m}Tc-labelled anti-LOX-1 [33] and ^{99m}Tc-MT1-MMP mAb successfully characterized these tracers. Further studies using these animal models should be helpful in the search for a suitable target molecule for imaging atherosclerotic plaques.

Conclusions

In this study, we succeeded in determining MT1-MMP expression in vivo utilizing a radiolabelled anti-MT1-MMP antibody and nuclear imaging techniques. Consequently, we demonstrated prominently higher accumulation of ^{99m}Tc-MT1-MMP mAb in grade IV atheroma. These findings indicate that nuclear imaging of MT1-MMP could provide new diagnostic imaging capabilities for characterizing atherosclerotic plaques, although further investigations to improve the blood clearance and target to blood ratios are strongly required.

Acknowledgments This work was partly supported by a Grant-in-Aid for General Scientific Research from the Ministry of Education, Culture, Sports, Science and Technology of Japan, and from the Japan Society for the Promotion of Science, and by a research grant from New Energy and Industrial Technology Development Organization (NEDO). This study was also partly supported by Special Coordination Funds for Promoting Science and Technology of the Ministry of Education, Culture, Sports, Science and Technology, the Japanese Government.

Conflicts of interest None.

References

1. Kolodgie FD, Virmani R, Burke AP, Farb A, Weber DK, Kutys R, et al. Pathologic assessment of the vulnerable human coronary plaque. Heart 2004;90:1385–91.
2. Lendon C, Born GV, Davies MJ, Richardson PD. Plaque fissure: the link between atherosclerosis and thrombosis. Nouv Rev Fr Hematol 1992;34:27–9.
3. Ruberg FL, Leopold JA, Loscalzo J. Atherothrombosis: plaque instability and thrombogenesis. Prog Cardiovasc Dis 2002;44:381–94.
4. Davies JR, Rudd JH, Weissberg PL. Molecular and metabolic imaging of atherosclerosis. J Nucl Med 2004;45:1898–907.
5. Jaffer FA, Libby P, Weissleder R. Molecular and cellular imaging of atherosclerosis: emerging applications. J Am Coll Cardiol 2006;47:1328–38.
6. Galis ZS, Khatri JJ. Matrix metalloproteinases in vascular remodeling and atherogenesis: the good, the bad, and the ugly. Circ Res 2002;90:251–62.
7. Galis ZS, Sukhova GK, Lark MW, Libby P. Increased expression of matrix metalloproteinases and matrix degrading activity in vulnerable regions of human atherosclerotic plaques. J Clin Invest 1994;94:2493–503.
8. Jones CB, Sane DC, Herrington DM. Matrix metalloproteinases: a review of their structure and role in acute coronary syndrome. Cardiovasc Res 2003;59:812–23.
9. Brown DL, Hibbs MS, Kearney M, Loushin C, Isner JM. Identification of 92-kD gelatinase in human coronary atherosclerotic lesions. Association of active enzyme synthesis with unstable angina. Circulation 1995;91:2125–31.
10. Li Z, Li L, Zielke HR, Cheng L, Xiao R, Crow MT, et al. Increased expression of 72-kd type IV collagenase (MMP-2) in human aortic atherosclerotic lesions. Am J Pathol 1996;148:121–8.
11. Davies JR, Rudd JH, Weissberg PL, Narula J. Radionuclide imaging for the detection of inflammation in vulnerable plaques. J Am Coll Cardiol 2006;47:C57–68.
12. Hartung D, Schäfers M, Fujimoto S, Levkau B, Narula N, Kopka K, et al. Targeting of matrix metalloproteinase activation for noninvasive detection of vulnerable atherosclerotic lesions. Eur J Nucl Med Mol Imaging 2007;34:S1–8.
13. Visse R, Nagase H. Matrix metalloproteinases and tissue inhibitors of metalloproteinases: structure, function, and biochemistry. Circ Res 2003;92:827–39.
14. Sato H, Takino T, Okada Y, Cao J, Shinagawa A, Yamamoto E, et al. A matrix metalloproteinase expressed on the surface of invasive tumour cells. Nature 1994;370:61–5.
15. Knäuper V, Bailey L, Worley JR, Soloway P, Patterson ML, Murphy G. Cellular activation of proMMP-13 by MT1-MMP depends on the C-terminal domain of MMP-13. FEBS Lett 2002;532:127–30.
16. Kuge Y, Takai N, Ishino S, Temma T, Shiomi M, Saji H. Distribution profiles of membrane type-1 matrix metalloproteinase (MT1-MMP), matrix metalloproteinase-2 (MMP-2) and cyclooxygenase-2 (COX-2) in rabbit atherosclerosis: comparison with plaque instability analysis. Biol Pharm Bull 2007;30:1634–40.
17. Rajavashisth TB, Xu XP, Jovinge S, Meisel S, Xu XO, Chai NN, et al. Membrane type 1 matrix metalloproteinase expression in human atherosclerotic plaques: evidence for activation by proinflammatory mediators. Circulation 1999;99:3103–9.
18. Stawowy P, Meyborg H, Stibenz D, Borges Pereira Stawowy N, Roser M, Thanabalasingam U, et al. Furin-like proprotein convertases are central regulators of the membrane type matrix

metalloproteinase-pro-matrix metalloproteinase-2 proteolytic cascade in atherosclerosis. Circulation 2005;111:2820–7.
19. Shiomi M, Ito T, Yamada S, Kawashima S, Fan J. Development of an animal model for spontaneous myocardial infarction (WHHLMI rabbit). Arterioscler Thromb Vasc Biol 2003;23:1239–44.
20. Abrams MJ, Juweid M, tenKate CI, Schwartz DA, Hauser MM, Gaul FE, et al. Technetium-99m-human polyclonal IgG radiolabeled via the hydrazino nicotinamide derivative for imaging focal sites of infection in rats. J Nucl Med 1990;31:2022–8.
21. Ono M, Arano Y, Mukai T, Uehara T, Fujioka Y, Ogawa K, et al. Plasma protein binding of (99m)Tc-labeled hydrazino nicotinamide derivatized polypeptides and peptides. Nucl Med Biol 2001;28:155–64.
22. Ono M, Arano Y, Uehara T, Yasushi F, Kazuma O, Namba S, et al. Intracellular metabolic fate of radioactivity after injection of technetium-99m-labeled hydrazino nicotinamide derivatized proteins. Bioconjug Chem 1999;10:386–94.
23. Larsen SK, Solomon HF, Caldwell G, Abrams MJ. [99mTc]tricine: a useful precursor complex for the radiolabeling of hydrazinonicotinate protein conjugates. Bioconjug Chem 1995;6:635–8.
24. Ishii K, Kita T, Kume N, Nagano Y, Kawai C. Uptake of acetylated LDL by peritoneal macrophages obtained from normal and Watanabe heritable hyperlipidemic rabbits, an animal model for familial hypercholesterolemia. Biochim Biophys Acta 1988;962:387–9.
25. Stary HC, Chandler AB, Dinsmore RE, Fuster V, Glagov S, Insull Jr W, et al. A definition of advanced types of atherosclerotic lesions and a histological classification of atherosclerosis. A report from the Committee on Vascular Lesions of the Council on Arteriosclerosis, American Heart Association. Circulation 1995;92:1355–74.
26. Stary HC, Chandler AB, Glagov S, Guyton JR, Insull Jr W, Rosenfeld ME, et al. A definition of initial, fatty streak, and intermediate lesions of atherosclerosis. A report from the Committee on Vascular Lesions of the Council on Arteriosclerosis, American Heart Association. Circulation 1994;89:2462–78.
27. Kobayashi S, Inoue N, Ohashi Y, Terashima M, Matsui K, Mori T, et al. Interaction of oxidative stress and inflammatory response in coronary plaque instability: important role of C-reactive protein. Arterioscler Thromb Vasc Biol 2003;23:1398–404.
28. Ishino S, Kuge Y, Takai N, Tamaki N, Strauss HW, Blankenberg FG, et al. 99mTc-Annexin A5 for noninvasive characterization of atherosclerotic lesions: imaging and histological studies in myocardial infarction-prone Watanabe heritable hyperlipidemic rabbits. Eur J Nucl Med Mol Imaging 2007;34:889–99.
29. Shiomi M, Ito T, Hirouchi Y, Enomoto M. Stability of atheromatous plaque affected by lesional composition: study of WHHL rabbits treated with statins. Ann N Y Acad Sci 2001;947:419–23.
30. Yun M, Yeh D, Araujo LI, Jang S, Newberg A, Alavi A. F-18 FDG uptake in the large arteries: a new observation. Clin Nucl Med 2001;26:314–9.
31. Zhao Y, Kuge Y, Zhao S, Morita K, Inubushi M, Strauss HW, et al. Comparison of 99mTc-annexin A5 with 18F-FDG for the detection of atherosclerosis in ApoE-/- mice. Eur J Nucl Med Mol Imaging 2007;34:1747–55.
32. Ogawa M, Ishino S, Mukai T, Asano D, Teramoto N, Watabe H, et al. (18)F-FDG accumulation in atherosclerotic plaques: immunohistochemical and PET imaging study. J Nucl Med 2004;45:1245–50.
33. Ishino S, Mukai T, Kuge Y, Kume N, Ogawa M, Takai N, et al. Targeting of lectinlike oxidized low-density lipoprotein receptor 1 (LOX-1) with 99mTc-labeled anti-LOX-1 antibody: a potential agent for imaging of vulnerable plaque. J Nucl Med 2008;49:1677–85.
34. Huhalov A, Chester KA. Engineered single chain antibody fragments for radioimmunotherapy. Q J Nucl Med Mol Imaging 2004;48:279–88.
35. Sharkey RM, Karacay H, Cardillo TM, Chang CH, McBride WJ, Rossi EA, et al. Improving the delivery of radionuclides for imaging and therapy of cancer using pretargeting methods. Clin Cancer Res 2005;11:7109s–21.
36. Watabe H, Ikoma Y, Kimura Y, Naganawa M, Shidahara M. PET kinetic analysis–compartmental model. Ann Nucl Med 2006;20:583–8.
37. Darambara DG, Todd-Pokropek A. Solid state detectors in nuclear medicine. Q J Nucl Med 2002;46:3–7.
38. Campean V, Neureiter D, Varga I, Runk F, Reiman A, Garlichs C, et al. Atherosclerosis and vascular calcification in chronic renal failure. Kidney Blood Press Res 2005;28:280–9.
39. Santoliquido A, Di Campli C, Miele L, Gabrieli ML, Forgione A, Zocco MA, et al. Hepatic steatosis and vascular disease. Eur Rev Med Pharmacol Sci 2005;9:269–71.
40. Beekman F, van der Have F. The pinhole: gateway to ultra-high-resolution three-dimensional radionuclide imaging. Eur J Nucl Med Mol Imaging 2007;34:151–61.
41. Akizawa H, Arano Y. Altering pharmacokinetics of radiolabeled antibodies by the interposition of metabolizable linkages. Metabolizable linkers and pharmacokinetics of monoclonal antibodies. Q J Nucl Med 2002;46:206–23.
42. Temma T, Sano K, Kuge Y, Kamihashi J, Takai N, Ogawa Y, et al. Development of a radiolabeled probe for detecting membrane type-1 matrix metalloproteinase on malignant tumors. Biol Pharm Bull 2009;32:1272–7.
43. Rogers BE, Anderson CJ, Connett JM, Guo LW, Edwards WB, Sherman EL, et al. Comparison of four bifunctional chelates for radiolabeling monoclonal antibodies with copper radioisotopes: biodistribution and metabolism. Bioconjug Chem 1996;7:511–22.
44. Sugimoto K, Nishimoto N, Kishimoto T, Yoshizaki K, Nishimura T. Imaging of lesions in a murine rheumatoid arthritis model with a humanized anti-interleukin-6 receptor antibody. Ann Nucl Med 2005;19:261–6.
45. D'Alessandria C, Malviya G, Viscido A, Aratari A, Maccioni F, Amato A, et al. Use of a 99mTc labeled anti-TNFalpha monoclonal antibody in Crohn's disease: in vitro and in vivo studies. Q J Nucl Med Mol Imaging 2007;51:334–42.
46. Cipollone F, Fazia M, Mezzetti A. Novel determinants of plaque instability. J Thromb Haemost 2005;3:1962–75.
47. Rudd JH, Hyafil F, Fayad ZA. Inflammation imaging in atherosclerosis. Arterioscler Thromb Vasc Biol 2009;29:1009–16.
48. Breyholz HJ, Wagner S, Levkau B, Schober O, Schäfers M, Kopka K. A 18F-radiolabeled analogue of CGS 27023A as a potential agent for assessment of matrix-metalloproteinase activity in vivo. Q J Nucl Med Mol Imaging 2007;51:24–32.
49. Schäfers M, Riemann B, Kopka K, Breyholz HJ, Wagner S, Schäfers KP, et al. Scintigraphic imaging of matrix metalloproteinase activity in the arterial wall in vivo. Circulation 2004;109: 2554–9.
50. Kolodgie F, Edwards S, Petrov A, Sachleben R, Hartung D, Weber DK. Noninvasive detection of matrix metalloproteinase upregulation in experimental atherosclerotic lesions and its abrogation by dietary modification [abstract]. Circulation 2001; 104:694.
51. Zhang J, Nie L, Razavian M, Ahmed M, Dobrucki LW, Asadi A, et al. Molecular imaging of activated matrix metalloproteinases in vascular remodeling. Circulation 2008;118:1953–60.
52. Fujimoto S, Hartung D, Ohshima S, Edwards DS, Zhou J, Yalamanchili P, et al. Molecular imaging of matrix metalloproteinase in atherosclerotic lesions: resolution with dietary modification and statin therapy. J Am Coll Cardiol 2008;52:1847–57.
53. Lancelot E, Amirbekian V, Brigger I, Raynaud JS, Ballet S, David C, et al. Evaluation of matrix metalloproteinases in atherosclerosis using a novel noninvasive imaging approach. Arterioscler Thromb Vasc Biol 2008;28:425–32.

SYNAPSE 65:77–83 (2011)

In Vivo Relationship Between Thalamic Nicotinic Acetylcholine Receptor Occupancy Rates and Antiallodynic Effects in a Rat Model of Neuropathic Pain: Persistent Agonist Binding Inhibits the Expression of Antiallodynic Effects

MASASHI UEDA,[1,2] YASUHIKO IIDA,[3] TOMOKI YONEYAMA,[2] TOMOKI KAWAI,[2] MIKAKO OGAWA,[4] YASUHIRO MAGATA,[4] AND HIDEO SAJI[2]*

[1]*Faculty of Medicine, Radioisotopes Research Laboratory, Kyoto University Hospital, Kyoto University, Kyoto 606-8507, Japan*

[2]*Department of Patho-Functional Bioanalysis, Graduate School of Pharmaceutical Sciences, Kyoto University, Kyoto 606-8501, Japan*

[3]*Faculty of Pharmaceutical Sciences, Clinical Analyzing Technology, Suzuka University of Medical Science, Suzuka 510-0293, Japan*

[4]*Laboratory of Genome-Bio Photonics, Photon Medical Research Center, Hamamatsu University School of Medicine, Hamamatsu 431-3192, Japan*

KEY WORDS thalamus; 5-[^{125}I]iodo-A-85380 ([^{125}I]5IA); desensitization

ABSTRACT We have recently clarified that nicotinic acetylcholine receptors (nAChRs) expressed in the thalamus play an important role in antiallodynic effects produced by the nAChR agonist, 5-iodo-3-(2(*S*)-azetidinylmethoxy)pyridine (5IA). This study aimed to reveal the in vivo relationship between thalamic nAChR occupancy rates and antiallodynic effects using 5IA and [^{125}I]5IA. We partially ligated the sciatic nerve of a rat to induce neuropathic pain. Antiallodynic effects were evaluated at 15, 30, 60, and 90 min after intracerebroventricular (i.c.v.) administration of multiple doses (1–100 nmol) of 5IA by the von Frey filament test. Receptor occupancy rates were measured by autoradiography at 15 and 90 min after administration. Antiallodynic effects of repetitive treatment of 5IA (5 and 50 nmol) were also examined. A significant and dose-dependent antiallodynic effect was observed 15 min after administration. It showed a good correlation with receptor occupancy rates (r = 0.97), indicating the binding of 5IA to nAChRs expressed in the thalamus involved in the antiallodynic effect. Five, 50, and 100 nmol of 5IA occupied the thalamic nAChRs until 90 min after administration, while the antiallodynic effect diminished. Five nanomoles of 5IA (which occupied 40% of thalamic nAChRs) showed a significant antiallodynic effect (percentage of the maximal possible effect (%MPE): 35 ± 7) after the second administration, while 50 nmol of 5IA (which occupied 80% of thalamic nAChRs) did not (%MPE: 7 ± 1). These findings suggest that not clearance of 5IA but desensitization of nAChRs caused by persistent binding of 5IA is responsible for the disappearance of antiallodynic effects. **Synapse 65:77–83, 2011.** ©2010 Wiley-Liss, Inc.

INTRODUCTION

Nicotinic acetylcholine receptors (nAChRs) are a family of ligand-gated ion channels that regulate neurotransmission in the central and peripheral nervous systems. The central nAChRs are pentameric complexes consisting of various α (α2–α10) and β (β2–β4) subunits, with the heteromeric α4β2 isoform being the most abundant nAChR subtype in the

Contract grant sponsor: Ministry of Education, Culture, Sports, Science and Technology of Japan (Grant-in-Aid for Scientific Research and Grant-in-Aid for Young Scientists); Contract grant numbers: 19209041, 19790869; Contract grant sponsor: Smoking Research Foundation

*Correspondence to: Hideo Saji, Department of Patho-Functional Bioanalysis, Graduate School of Pharmaceutical Sciences, Kyoto University, 46-29 Yoshida Shimoadachi-Cho, Sakyo-Ku, Kyoto 606-8501, Japan. E-mail: hsaji@pharm.kyoto-u.ac.jp

Received 28 October 2009; Accepted 30 April 2010

DOI 10.1002/syn.20819

Published online 19 May 2010 in Wiley Online Library (wileyonlinelibrary.com).

mammalian brain (Dwoskin et al., 2009). Indeed, it has been suggested that at least 90% of neuronal nAChRs in the brain are α4β2 nAChRs (Flores et al., 1992; Lindstrom et al., 1995). The homomeric α7 isoform is the second most abundant nAChR subtype in the brain. These receptors are implicated not only in various brain functions, such as cognition, memory and learning, but also in many diseases, e.g., Alzheimer's disease (Court et al., 2000; Paterson and Nordberg, 2000). Thus, clarifying how nAChRs are associated with physiological or pathological function has been of great interest.

5-[$^{123/125}$I]iodo-3-(2(*S*)-azetidinylmethoxy)pyridine ([$^{123/125}$I]5IA) is one of the tools that can make such researches possible. This compound is a radiolabeled form of 5IA, which is a derivative of A-85380, iodinated at the 5-position of the pyridine ring. [$^{123/125}$I]5IA is a nAChR imaging probe with high selectivity and specificity for α4β2 nAChRs not only in rodents but also in humans (Mamede et al., 2004; Ogawa et al., 2009), and it has a relatively good safety profile (Brasic et al., 2009; Ueda et al., 2004). In fact, some methodologies have been developed for the noninvasive imaging and quantification of nAChR density in vivo (Fujita et al., 2003; Mamede et al., 2004; Staley et al., 2005). By using these techniques, changes in the nAChR density of living humans have been found, e.g., decrease in Alzheimer's disease and Parkinson's disease (Mitsis et al., 2009b; Oishi et al., 2007); age-related decline (Mitsis et al., 2009a); and upregulation and recovery after smoking cessation (Mamede et al., 2007; Mukhin et al., 2008).

Moreover, 5IA acts as a nAChR agonist, and a neuroprotective effect and an analgesic effect of 5IA have been reported (Ueda et al., 2008; Ueda et al., 2010). The biodistribution and metabolism of [$^{123/125}$I]5IA are both similar to those of 5IA because [$^{123/125}$I]5IA is a radiolabeled analog of 5IA. Accordingly, pharmacokinetics, receptor occupancy, and binding potential (BP) (an index of nAChR density) of 5IA can be easily measured using [$^{123/125}$I]5IA. Studies using 5IA have the advantage of pharmacodynamic effects being directly compared to the pharmacokinetic profile of the compound.

Recently, we demonstrated an upregulation of thalamic nAChRs in a rat model of chronic pain. Moreover, we found that intrathalamic administration of 5IA attenuated tactile allodynia in a dose-dependent manner and that the blockade of thalamic nAChRs reduced the antiallodynic effect of 5IA administered by an intracerebroventricular (i.c.v.) route (Ueda et al., 2010). These findings indicate that thalamic nAChRs are potentially where the antinociceptive action of 5IA is produced. Therefore, we focused on nAChRs in the thalamus and aimed to reveal the in vivo relationship between thalamic nAChR occupancy rates and antiallodynic effects in a rat model of neuropathic pain. Since it has been reported that A-85380 acts on both peripheral and central nAChRs, and shows antiallodynic effects after i.p. administration (Rueter et al., 2003), we adopted i.c.v. administration instead of systemic administration in order to evaluate the antiallodynic effect associated only with thalamic nAChRs. The similarity between 5IA and [$^{123/125}$I]5IA has a great advantage that enables us to evaluate the relationship between pharmacological effects and receptor occupancy directly and with great precision. In this study, we measured the occupancy rates of thalamic nAChRs by 5IA and compared the results with antiallodynic effects.

MATERIALS AND METHODS

Animals

Animal experiments were conducted in accordance with our institutional guidelines. Experimental procedures were approved by the Kyoto University Animal Care Committee.

Male Sprague-Dawley rats weighing 200–250 g were purchased from Japan SLC (Hamamatsu, Japan). The animals were kept at a constant ambient temperature under a 12-h light/dark cycle with free access to food and water.

Reagents

Iodine-125 radionuclide was purchased from PerkinElmer (Waltham, MA). (−)-Cytisine was purchased from Sigma-Aldrich (St. Louis, MO). 5IA and [^{125}I]5IA were synthesized according to a previously published method (Saji et al., 2002). The specific radioactivity of [^{125}I]5IA was determined from the UV absorbance at 254 nm as more than 55 GBq/μmol (the limit with detection of this method). Drugs were administered to animals as physiological saline solution. All other chemicals used were of reagent grade.

Surgical operation

Neuropathic pain was established by a partial sciatic nerve ligation (PSL) according to a previously published method (Seltzer et al., 1990; Ueda et al., 2010). Under sodium pentobarbital anesthesia (50 mg/kg, intraperitoneally [i.p.]), the right sciatic nerve was exposed just distal to the branch leading to the posterior biceps femoris/semitendinosus muscles. A 7-0 silk suture was inserted into the nerve and tightly ligated so that the dorsal 1/3–1/2 of the nerve was trapped in the ligature.

After recovery from PSL surgery, the rats were implanted with a stainless steel guide cannula (outside diameter [o.d.] 0.7 mm, inside diameter [i.d.] 0.38 mm) under sodium pentobarbital (50 mg/kg, i.p.) anesthesia for i.c.v. administration. The rats were placed into a stereotaxic apparatus (SR-5, Narishige, Tokyo, Japan) and unilaterally implanted with a